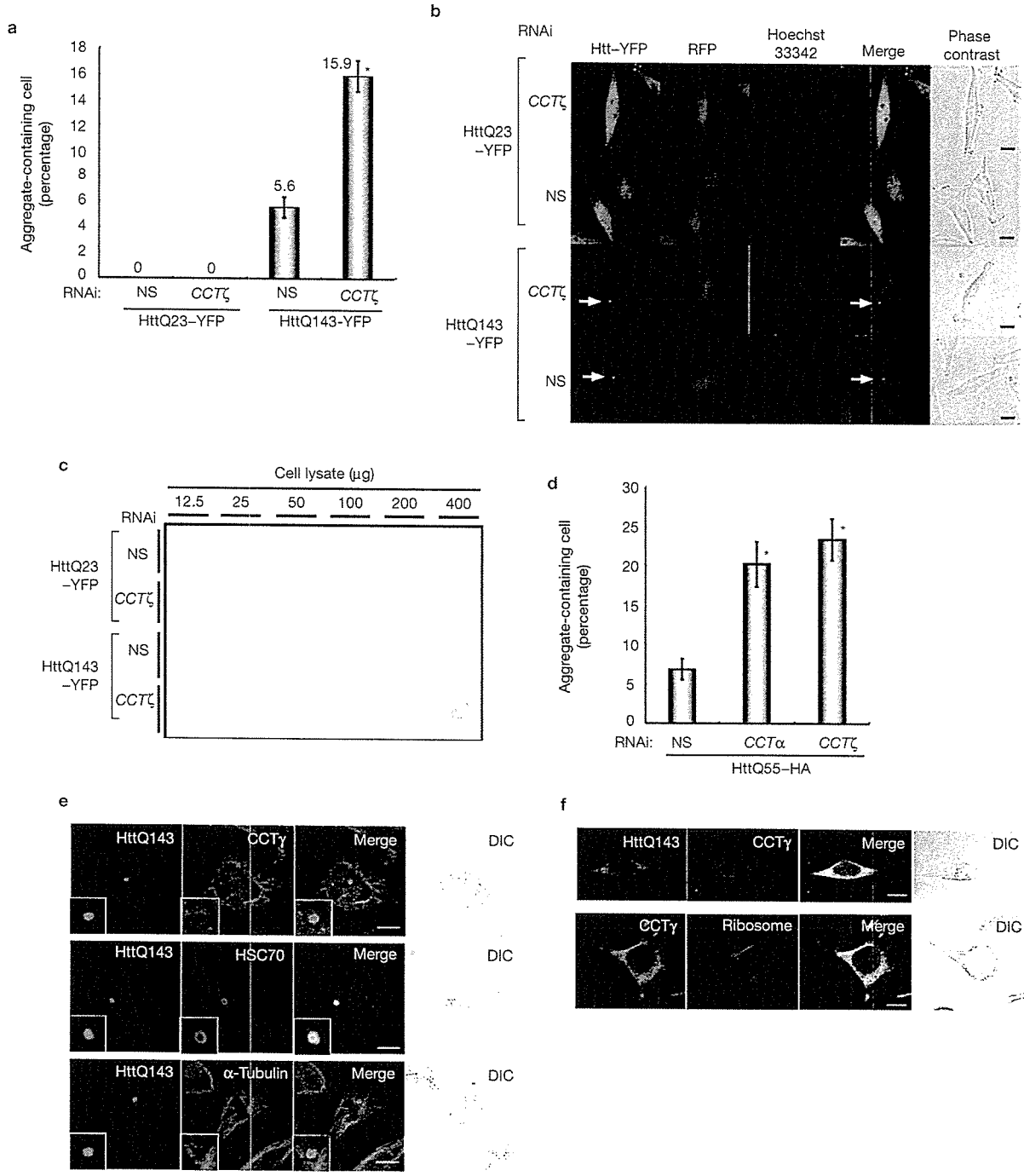

Figure 2 CCT is required for preventing Htt aggregation in stable transformants of HeLa cells. (**a**) *CCTζ* depletion increases number of cells containing HttQ143–YFP aggregates. Cells were cotransfected with vectors for *CCTζ* RNAi and mRFP1 expression as a transfection marker, and Htt–YFP expression was simultaneously induced by removal of tetracycline from the medium. Cells containing YFP-aggregates were counted and their percentage in RFP signal-emitting cells were determined. ($n = 3$) (**b**) Fluorescent images of aggregated HttQ143–YFP and diffusely distributed HttQ23–YFP in *CCTζ* depleted and control cells. Arrows indicate aggregates. The scale bar represents 20 μm. (**c**) Filter-trap assay of Htt–YFP aggregates in *CCTζ* -depleted and control cells. (**d**) Aggregation of HttQ55–HA is stimulated by depletion of *CCTα* or *CCTζ* . Cells were cotransfected with expression vectors of HttQ55–HA and *CCT* subunit RNAi vectors, and stained with anti-HA antibody after fixation. Percentages of aggregate positive cells are shown. ($n = 3$) (**e**) Cells with visible HttQ143 inclusions were stained with antibodies against CCTγ, HSC70 or α-tubulin and AlexaFluor 594-conjugated secondary antibody. Insets correspond to enlarged view of aggregates. (**f**) Cells with no visible inclusion were stained using antibodies against GFP (for HttQ143–YFP), CCTγ and ribosome. The scale bar represents 10 μm. The asterisk indicates P 0.01. The error bars in **a** and **d** represent s.d.

©2006 Nature Publishing Group

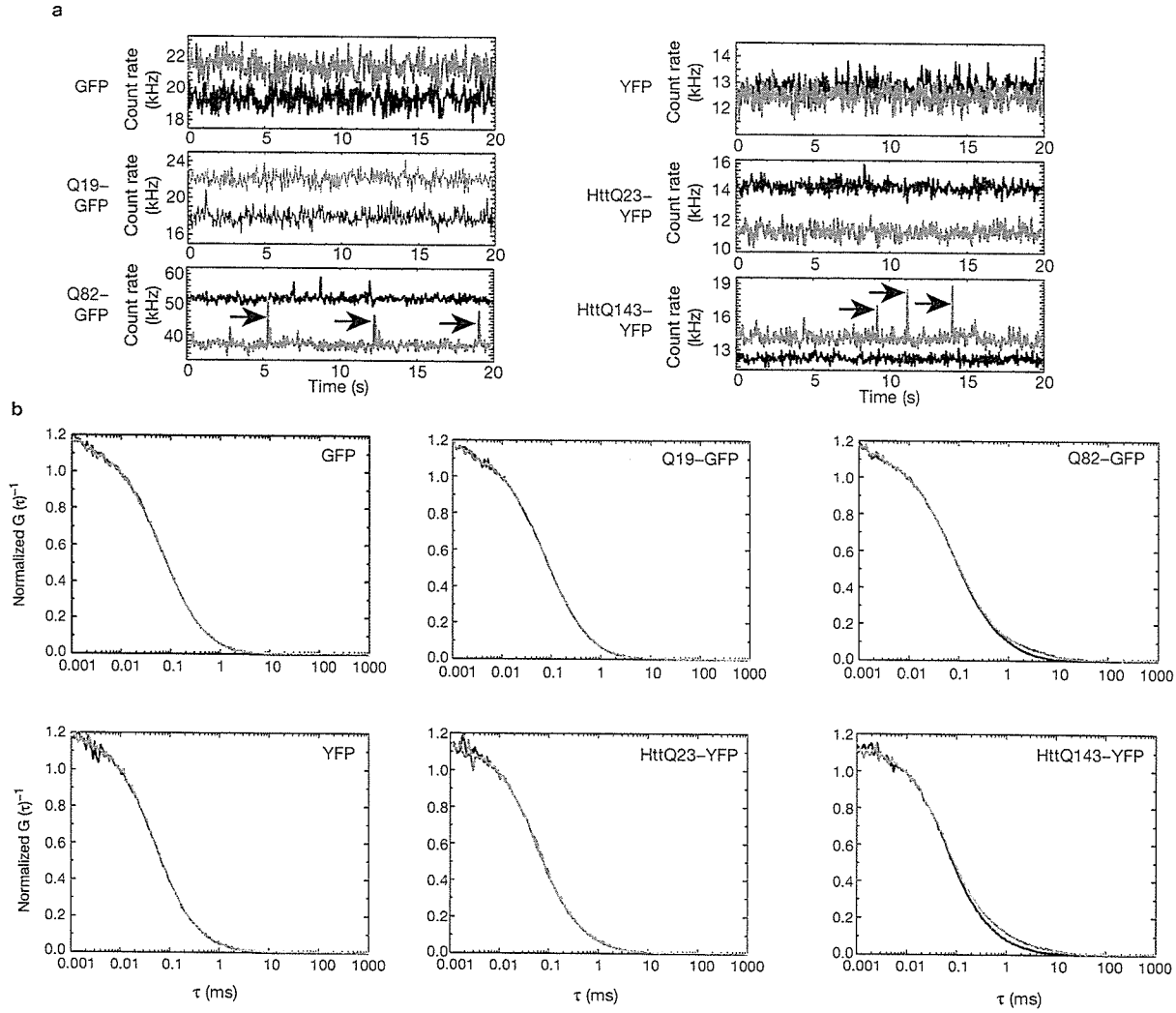

Figure 3 Depletion of CCT subunits stimulates formation of soluble aggregates of polyQ-expansion proteins. (**a**, **b**) GFP, Q19–GFP or Q82–GFP were transiently expressed in HEK293 cells in the presence of *CCTζ* RNAi vector or nonspecific RNAi vector. Alternatively, expression of YFP, HttQ23–YFP or HttQ143–YFP were induced in HeLa stable cell lines in the presence of *CCTζ* RNAi or nonspecific RNAi vectors. After 72 h of expression, cells were lysed in PBS. Supernatant recovered after centrifugation (10,000*g*) were analysed by fluorescence correlation spectroscopy. Count rates of fluorescence in *CCTζ* depleted (red) and control (blue) cell lysates during 20 s measurements are shown in **a**. Arrows indicate slowly diffusing bright molecules that were passing through the confocal volume. Correlation curves of Htt–polyQ proteins in *CCTζ* depleted (red) and control (blue) cell lysates are shown in **b**.

knockdown of the subunit. Except for a slight reduction of the levels of CCTα and CCTε subunits, no significant effect of *CCTζ* knockdown was observed on the levels of the other subunits, indicating reasonably selective knockdown of the ζ subunit. Reduction in the levels of the ζ subunit did not affect overall cell morphology or cell-growth rates of transfected cells under the conditions described (data not shown). However, depletion of the ζ subunit did significantly reduce the levels of the CCT complex detected by sucrose density gradient analysis. In *CCTζ*-depleted cells, the majority (82%) of the CCT subunits were monomers or small oligomers, whereas in untreated cells essentially only the high molecular weight CCT complexes (96,000) were detected (Fig. 1b). The CCT complex was also disrupted by CCTα subunit depletion in HEK293 cells (see Supplementary Information, Fig. S1a, b) and by CCTζ depletion in HeLa cells (see Supplementary Information, Fig. S2a, b). Taken together, these results indicate that human cells depleted for the CCTζ subunit have reduced levels of CCT.

To examine whether reduction of CCT affected polyQ aggregation and toxicity phenotypes, we expressed different lengths of polyQ repeats fused with YFP (YFP, Q19–YFP and Q82–YFP) in HEK293 cells with the *CCTζ* siRNA vector or nonspecific siRNA vector. Following transfection, the fraction of aggregate-containing cells was monitored by fluorescent microscopy. A low level (10.9%) of the Q82–YFP transfected cells exhibited aggregates similar to previous observations[20]. On *CCTζ* depletion, there was a 2.5-fold increase in aggregate containing cells (Fig. 1c). In contrast, no effect of *CCTζ* depletion was observed in cells expressing either Q19–YFP or YFP alone. It was also confirmed that the nonspecific RNAi vector exhibits no significant difference to a scrambled *CCTζ* RNAi control vector for the levels of CCTζ protein and polyQ aggregation (see Supplementary Information, Fig. S1c, d). In addition, we examined whether depletion of other CCT subunits affected polyQ aggregation by RNAi knockdown and found that depletion of *CCTα* significantly stimulates Q82–GFP aggregation (Fig. 1d). These results

©2006 Nature Publishing Group

Table 1 Diffusion constants of Htt-polyQ proteins under *CCT*-depleted and normal conditions

		Rapid fraction (F1)		Slow fraction (F2)				
	RNAi	Diffusion time (μs)	Content (percentage)	Diffusion time (μs)	Content (percentage)	χ^2	D_{F1} (μm² s⁻¹)	D_{F2} (μm² s⁻¹)
GFP	*NS*	70.7 ± 1.5	100	–	–	1.19 ± 1.76 × 10⁻⁶	85.8 ± 0.8	–
GFP	*CCTζ*	70.7 ± 2.1	100	–	–	1.67 ± 2.61 × 10⁻⁶	85.9 ± 1.9	–
Q19–GFP	*NS*	86.3 ± 4.0	100	–	–	7.43 ± 11.33 × 10⁻⁷	70.3 ± 2.8	–
Q19–GFP	*CCTζ*	86.0 ± 3.6	100	–	–	5.24 ± 8.45 × 10⁻⁷	70.6 ± 2.0	–
Q82–GFP	*NS*	86.0[a]	95.4± 0.9	1122 ± 416	4.6 ± 0.9	7.56 ± 2.10 × 10⁻⁷	71.6 ± 1.9[b]	8.3 ± 3.7
Q82–GFP	*CCTζ*	86.0[c]	91.3 ± 2.4	4255 ± 1920	8.7 ± 2.4	1.84 ± 0.12 × 10⁻⁶	71.6 ± 1.9[b]	3.0 ± 1.8
YFP	*NS*	77.7 ± 3.1	100	–	–	3.22 ± 0.24 × 10⁻⁶	84.2 ± 1.5	–
YFP	*CCTζ*	78.3 ± 3.5	100	–	–	5.13 ± 3.37 × 10⁻⁶	83.5 ± 2.1	–
HttQ23–YFP	*NS*	147.3 ± 1.5	100	–	–	6.76 ± 3.53 × 10⁻⁶	44.3 ± 1.3	–
HttQ23–YFP	*CCTζ*	147.7 ± 3.1	100	–	–	6.61 ± 1.83 × 10⁻⁶	44.3 ± 1.5	–
HttQ143–YFP	*NS*	150.0[a]	98.8 ± 0.4	4859 ± 1897	1.2 ± 0.4	1.71 ± 2.55 × 10⁻⁵	43.6 ± 1.1[b]	1.5 ± 0.7
HttQ143–YFP	*CCTζ*	150.0[c]	93.5 ± 1.5	5493 ± 2540	6.5 ± 1.5	3.73 ± 2.16 × 10⁻⁶	43.6 ± 1.1[b]	1.3 ± 0.5

Diffusion time and constant (D) were estimated by curve fitting of the polyQ–GFP or Htt–YFP FCS data at 72 h (mean ± s.d. of three independent experiments). The deviations of diffusion constant were derived from difference between measured samples and variance of the diffusion time of Rh6G used as a standard (see Methods). The data of GFP, Q19–GFP, YFP and HttQ23–YFP were analysed by one component model whereas the Q82–GFP and HttQ143–YFP data were analysed by two component model to provide the best fit. Significance of curve fitting was analyzed by χ^2 test. [a]To accurately estimate the diffusion time and content of the second component (soluble aggregates) at 72 h, the diffusion time of the first component was fixed to the values of monomers that were determined at 24 h. [b]The variance of D values was provided from variance of the diffusion time of Rh6G used as a standard whereas the diffusion time of the first component was fixed.

indicate that the effect of knockdown of different subunits of CCT is an enhancement of polyQ aggregation. These observations are consistent with the fact that all eight subunits are essential to form functional chaperonin complex.

The morphological characteristics of Q82–YFP inclusions observed in *CCTζ* knockdown cells were indistinguishable from control Q82–YFP expressing cells in terms of the numbers of aggregate structures per cell, aggregate size or perinuclear localization (Fig. 1e). Consistent with the observed increase in the number of cells with aggregates, cellulose-acetate filter-trap assay of cell lysates indicated that the cells depleted of *CCT* have increased levels of Q82–YFP aggregates (1.7-fold), whereas cells expressing either Q19–YFP or YFP alone did not form aggregates, even after *CCTζ* knockdown (Fig. 1f).

We next examined whether changes in the levels of CCT influenced Htt phenoytpes using HeLa cells stably expressing HttQ143–YFP or HttQ23–YFP under the control of Tet-off system. In HttQ143–YFP cells transfected with the *CCTζ* knockdown vector (transfected cells were identified by cotransfection with mRFP1 vector), the fraction of cells with aggregates increased 2.8-fold (Fig. 2a). Aggregate size and morphology was unaltered (Fig. 2b) similar to previous reports[20,21]. Consistent with the observed increase in numbers of aggregate-containing cell numbers, a 7.5-fold increase in aggregated Htt protein levels was detected by the filter trap assay (Fig. 2c). Aggregation of HttQ55 fused with a HA tag consisting of only ten amino acids was also stimulated by depletion of each of two different subunits tested (Fig. 2d and see Supplementary Information, Fig. S2c), confirming that the stimulation of Htt aggregation by depletion of specific CCT subunits was not influenced by the heterologous presence of the YFP (GFP) tag. Thus, CCT is required to prevent the aggregation of polyQ-expansion proteins, including Htt.

It has been shown previously that Hsp70 inhibits polyQ aggregation *in vitro* and *in vivo*[22,23]. Hsp70 colocalizes to Htt–polyQ aggregates and exhibits dynamic interactions in human cells unlike other associated cellular proteins that are stably sequestered[24]. We therefore examined the subcellular localization of CCT in Htt aggregate-containing cells by immunostaining and detected the diffuse distribution of CCT throughout the cytosol, but not in association with visible Htt inclusions (Fig. 2e). Similar results were obtained for Q82–YFP inclusions (see Supplementary Information, Fig. S1e). These results are consistent with the distinct chaperone activities between CCT and Hsp70. As CCT functions as a cage for folding reactions, we postulate that CCT is diffusely distributed in the cytosol in proximity of translating ribosomes. Consistent with this notion, colocalization of CCT with soluble HttQ143–YFP and ribosomes was observed in cells with no visible inclusion (Fig. 2f). Thus, CCT may affect aggregation process of Htt at an earlier soluble stage.

To address how CCT influences polyQ aggregation states, we employed dynamic imaging methods. Fluorescence recovery after photobleaching (FRAP) analysis did not reveal any differences in the mobility of polyQ–GFP on depletion of CCT (see Supplementary Information, Fig. S3), therefore we turned to fluorescence correlation spectroscopy, a method developed for the analysis of rapid movement of fluorescent molecules at near single molecule levels[25,26]. After cotransfection of HEK293 cells with polyQ–GFP and RNAi vectors for 72 h, cell extracts were prepared and the soluble fractions were analysed by fluorescence correlation spectroscopy. The record of fluorescent fluctuation indicated that significant numbers of slowly diffusing bright molecules were passing through the confocal volume in the soluble fraction prepared from cells expressing Q82–GFP or HttQ143–YFP under CCT depleted conditions (Fig. 3a). The shift of correlation curves to larger diffusion times of Q82–GFP by *CCTζ* depletion indicates that molecular sizes of the polyQ protein have become significantly larger as the levels of CCT are reduced (Fig. 3b). In contrast, Q19–GFP or GFP alone exhibited no significant difference in diffusion on CCT depletion. Curve fitting of these data (Table 1) indicates that a fraction of Q82–GFP (F2) diffuses much more slowly than monomer fractions (F1), even in the untreated cells. The diffusion constants of these fractions indicate that the slow fraction diffuses eightfold (or greater) more slowly than monomers and that the content of the slow fraction was increased by twofold (8.7% versus 4.6%) after *CCTζ* knockdown. Similarly, an increase in diffusion mobility in the

©2006 Nature Publishing Group

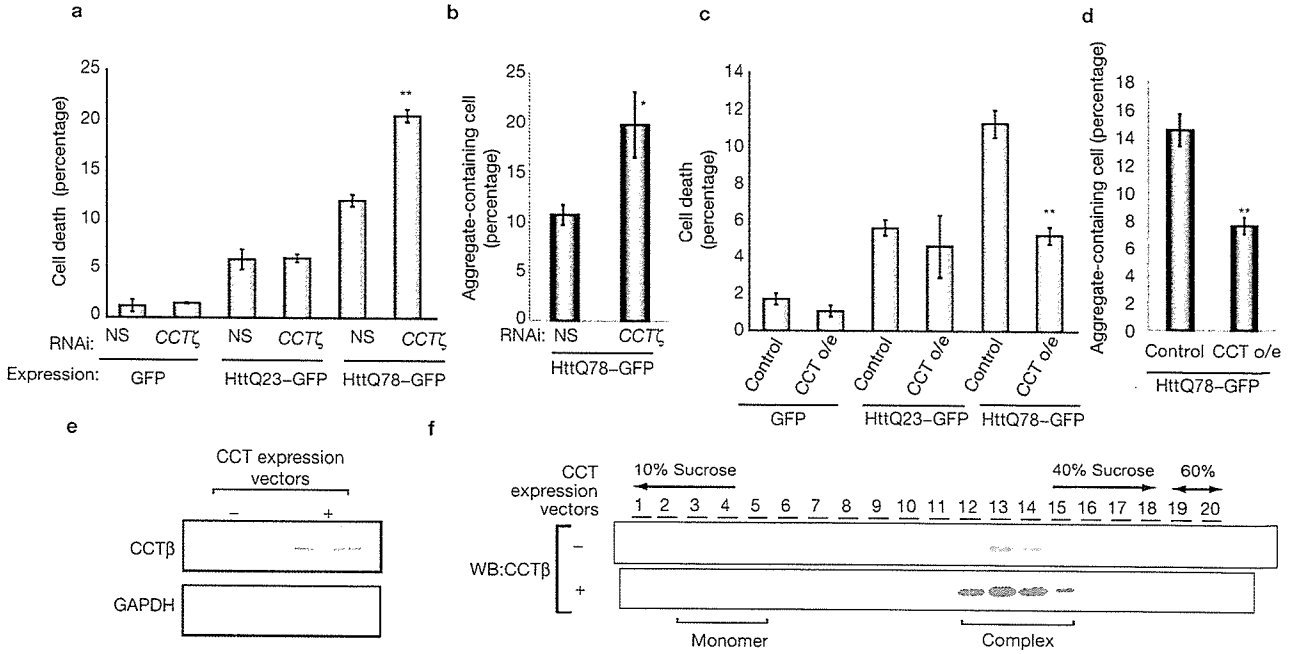

Figure 4 CCT prevents Htt toxicity and aggregation in neuronal cells. (a) *CCTζ* depletion enhances Htt-induced neuronal cell death. Mouse Neuro2a cells were transfected with Htt–GFP expression vector along with *CCTζ* RNAi or nonspecific RNAi vectors. Cells were stained by propidium iodide to monitor cell death and percentage in GFP expressing cells were calculated ($n = 3$). (b) *CCTζ* depletion enhances Htt aggregation in Neuro2a cells ($n = 3$). (c) CCT overexpression reduces Htt-induced neuronal cell death. Neuro2a cells were cotransfected with expression vectors of Htt–GFP and all eight CCT subunits. o/e, overexpression. (d) CCT overexpression reduces Htt aggregation in Neuro2a cells ($n = 3$). (e) Neuro2a cells were transfected with expression vectors of all eight CCT subunits and total proteins extracted were analysed by western blotting. (f) The extracts described in e were fractionated by sucrose gradient centrifugation and subsequently analysed by western blotting using anti-CCTβ antibody. Single asterisk indicates P 0.05; double asterisk indicates P 0.01. The error bars represnt s.d.

soluble fraction of HttQ143–YFP expressing HeLa cells was observed, whereas HttQ23–YFP and YFP showed no difference (Fig. 3b). The diffusion of the slow fraction of HttQ143–YFP was 30-fold slower than monomers and its relative content was increased significantly (1.2% to 6.5%) by CCT depletion (Table 1). In contrast, no difference of diffusion mobility was observed at earlier times of 24 or 48 h (see Supplementary Information, Fig. S4). The slow fraction of Q82–YFP or HttQ143–YFP thus appeared within the last 24 h of the 72 h RNAi treatment, corresponding to the same period when visible aggregates formed (no aggregates were observed at 24 and 48 h treatment, data not shown). Soluble aggregates of Q82–GFP were also detected in CCT-depleted cells using sucrose gradient centrifugation followed by western blotting, whereas they were hardly detected in control cells probably due to the detection limit of the method (see Supplementary Information, Fig. S1f). Taken together, these data support the hypothesis that inhibition of CCT function enhances the appearance of soluble Htt–polyQ aggregates leading to the formation of visible inclusions.

To examine whether changes in the level of CCT also affected Htt–polyQ-induced neuronal cell death, Htt was expressed in Neuro2a cells where CCT subunits were depleted. Reduction of CCT subunits resulted in a near doubling of polyQ expansion-dependent cell death (Fig. 4a), together with a twofold stimulation of aggregation (Fig. 4b). We next asked whether overexpression of CCT subunits would suppress Htt–polyQ aggregation and cytotoxicity. To achieve increased expression of the CCT complex, Neuro2a cells were cotransfected with expression vectors for all eight CCT subunits (Fig. 4e, f). This resulted in a significant inhibition of HttQ78 aggregation in Neuro2a cells (Fig. 4d) and polyQ82 aggregation in HEK293 cells (see Supplementary Information, Fig. S1g). In contrast, overexpression of only a single subunit of CCT had no effect on polyQ82 aggregation (see Supplementary Information, Fig. S1h). Simultaneous overexpression of all eight CCT subunits reduced cell death of the Neuro2a expressing HttQ78 by more than 50% (Fig. 4c), thus indicating that CCT has a positive protective role against the cytotoxicity of polyQ-expansion proteins like Htt.

Here, we have shown that changes in the levels of the cytosolic chaperonin CCT affect the aggregation state and toxicity of Htt–polyQ proteins in mammalian cells. RNAi knockdown of *CCT* subunits disrupt the CCT complex and consequently blocks its ability to trap substrates[16,17]. Intriguingly, our fluorescence correlation spectroscopy experiments revealed that depletion of CCT subunits results in the appearance of soluble polymeric Htt–polyQ species, whereas *CCT* knockdown does not alter size or morphology of finally formed visible aggregates. Thus, CCT seems to inhibit aggregate formation at an earlier soluble stage.

Using an *in vitro* translation system reconstituted with purified proteins, we recently demonstrated that CCT prevents aggregation of newly synthesized Gβ[19], a WD40 repeat protein very rich in β-sheets. Detailed analysis of the CCT binding regions in Gβ revealed that CCT specifically recognize hydrophobic β-strands. Thus, a specific function of CCT may be to protect against aggregation of hydrophobic β-sheets. Consistent with this proposal, CCT has been shown to bind hydrophobic β-strands in VHL[27] and interact with the WD40 family β-sheet rich proteins *in vivo*[28]. As polyQ repeats are known to form β-sheet structures in aggregates, CCT may be essential for trapping β-sheet structures required for aggregate formation.

©2006 Nature Publishing Group

HSP70 has been shown to prevent Htt-polyQ aggregation *in vitro*[22] and transiently interacts with visible aggregates *in vivo*[23]. In contrast, we show here that CCT subunits do not concentrate in the visible Htt-polyQ aggregate structure but rather remain localized throughout the cytosol. As CCT functions as a cage-like machine that assists in folding of substrates by trapping them within the cavity, the structure of CCT may prevent association with large insoluble inclusions. Our data from fluorescence correlation spectroscopy analysis supports this hypothesis because CCT affects the formation of soluble aggregates but not of the large visible aggregates. Although we do not know the exact mechanism by which CCT affects polyQ folding, these observations suggest a biochemical process that is distinct from the mechanisms proposed for Hsp70 interaction with unfolded and partially folded substrates. Differences in the levels of the Hsp70 and CCT chaperones could therefore influence aspects of cell type sensitivity to the stress of misfolded proteins.

Overexpression of the CCT complex has a significant inhibitory effect on the aggregation and cytotoxicity of Htt-polyQ in mammalian cells. Therefore, modulation of CCT function may offer an approach to prevent neurodegenerative disorders caused by protein aggregation including polyQ diseases. □

Note added proof: a related manuscript by Tam et al. (Nature Cell Biol. *8, doi: 10.1038/ncb1477; 2006) is also published in this issue.*

METHODS

Constructs. Plasmid vectors expressing siRNAs for 21-nucleotide target sequences of human *CCTζ-1* mRNA (AAGTCTGTGGCGATTCAGATA), human *CCTα* mRNA (AAATACTAAGGCTCGTACGTC) and mouse *CCTζ-1* mRNA (AAGTCTGTGGTGACTCAGATA) were constructed using pSUPER (OligoEngine, Seattle, WA). A non-silencing control vector expressing non-specific siRNA (NS-pSUPER) was obtained from Dharmacon, Lafayette, CO. Expression vectors for polyQ-EYFP and polyQ-EGFP were described previously[20,21]. Expression vectors for Htt-exon-1 fused with EYFP were produced as previously described[21] and the *Htt-exon-1* gene inserts were then subcloned into pEGFP-N1 (Invitrogen, Carlsbad, CA) for Htt-EGFP expression vectors. mRFP1 expression vector was constructed by excising the mRFP1 insert from mRFP1-pRsetB[29] and subcloned into pEGFP-C1 vector after removing the EGFP segment. For overexpression of eight CCT subunits, human cDNAs of individual subunits were separately cloned into pCAGGS expression vector.

Cell culture, transfection and biochemical analysis. HEK293, HeLa and Neuro2a cells were cultured in DMEM supplemented with 10% foetal bovine serum. HeLa stable cell lines carrying Tet-off-regulated *Htt-EYFP* genes were cloned and maintained as previously described[21]. HEK293, HeLa and Neuro2a cells were transfeceted using Lipofectamine 2000, Optifect (Invitrogen) and Effectene (Qiagen, Dusseldorf, Germany), respectively. For the HeLa stable cell lines, they were cotransfected with mRFP1 and other plasmids, and cells emitting red colour signals for mRFP1 were considered transfected cells. Determination of protein concentration, western blotting analysis and sucrose gradient fractionation were performed as previously described[30]. For CCT subunit overexpression experiments, Neuro2a cells (3.5-cm dish) were transfected with the eight CCT subunit expression vectors (10 ng each), Htt-GFP (100 ng) and empty pCAGGS (320 ng). For control experiments, the CCT subunit expression vectors were replaced by the same amount of empty pCAGGS.

Analysis of aggregate-containing cells. Cells were grown on coverslips coated with poly-L-lysine for HEK293 cells, type I collagen for HeLa cellsor type IV collagen for Neuro2A cells, respectively. At 72 h after transfection, cells were fixed with 4% paraformaldehyde in PBS for 15 min and stained with Hoechst 33342. Images were taken by an Axioplan2 microscope with Plan-NeoFluar 40× 0.75 NA objective (Carl Zeiss, Jena, Germany).

Analysis of cell death. Neuro2a cells were grown on φ27 glass-bottom dish coated with type IV collagen for 16 h. Immediately after transfection of Htt-GFP expression vectors, neuronal cell differentiation was induced by addition of 5 mM dibutyryl cAMP for 72 h. Cells stained with propidium iodide (1 μg ml^{-1}) were counted as dead cells using a Biozero digital microscope (Keyence, Osaka, Japan) through a PlanFluor 10× 0.30 NA objective (Nikon, Tokyo, Japan).

Filter-trap assay. Cells were lysed in PBS containing 0.5% Triton X-100 and protein concentrations were determined. Lysates were diluted in 1% SDS-PBS and boiled for 5 min. Immediately after cooling, samples were loaded onto cellulose acetate membrane (0.2 μm) settled on a dot blotter (Bio-Rad, Hercules, CA). After blocking with 1% skim milk and 0.05% Tween 20 in PBS overnight, the membrane was incubated with mouse anti-GFP antibody (GA200, Nacalai Tesque, Kyoto, Japan) and alkaline-phosphatase conjugated anti-mouse IgG antibody (Biosource, Camarillo, CA). Alkaline-phosphatase activity was detected by developing in NBT-BCIP (nitro-blue tetrazolium chloride and 5-bromo-4-chloro-3′-indolyl-phosphatase *p*-toluidine salt) solution (Sigma-Aldrich, St Louis, MO).

Immunofluorescence microscopy. Cells grown on coverslips were fixed in methanol at −20 °C for 5 min or 4% paraformaldehyde in PBS at 37 °C for 15 min and washed three times in PBS. After treatment with 0.5% Triton X-100 and 0.5% saponin in PBS for 5 min, cells were blocked with 1% BSA, 10% glycerol and 0.02% Triton X-100 in PBS. Cells were incubated with rabbit anti-CCTγ antibody (1:50), rat anti-HSC70 antibody (1:100, SPA-815, Stressgen, Ann Arbor, MI), mouse anti-α-tubulin antibody (1:200, DM1A, CalbioChem, San Diego, CA), mouse anti-GFP antibody (1:100), or goat anti-ribosomal protein L11 (1:50, sc-25931, SantaCruz, Santa Cruz, CA) and then with AlexaFluor 488 or 594 conjugated anti-rabbit, rat, goat, or mouse IgG (1:200, Molecular Probes, Carlsbad, CA). At the second antibody incubation, cells were costained with 1.0 μg ml^{-1} Hoechst 33342 for nuclear staining. Images were collected by LSM 510 META confocal microscope through a Plan-Apochromat 63× 1.4 NA oil-immersion objective (Carl Zeiss). The pinhole aperture for Hoechst, YFP and Alexa594 channels were settled at 84 μm, 94 μm and 127 μm, respectively.

Fluorescence correlation spectroscopy analysis. Fluorescence correlation spectroscopy measurements were performed by a ConfoCor 2 system with C-Apochromat 40× 1.2NA water immersion objective lens (Carl Zeiss). EGFP and EYFP were excited at 488 nm and 514 nm, respectively. Confocal pinhole diametres were adjusted to 70 μm at 488 nm, or 74 μm at 514 nm. Emission signals were detected by a 505 nm long-pass filter for EGFP or a 530–600 nm band-pass filter for EYFP. Cells (3.5-cm dish) were lysed in 0.2 ml PBS by passing through a 27 gauge needle and the supernatant was recovered after centrifugation (10,000*g*, 2 min) and diluted appropriately. Fluorescence signals of the supernatant were recorded on Lab-Tek 8-well chamber slides at 25 °C. The fluorescence autocorrelation functions, $G(\tau)$, from which the average residence time (τ_i) and the absolute number of fluorescent proteins in the detection volume are calculated, are obtained as follows:

$$G(\tau) = \frac{\langle I(t)\, I(t+\tau)\rangle}{\langle I(t)\rangle^2}$$

where $I(t+\tau)$ is the fluorescence intensity obtained by the single photon counting method in a detection volume at a delay time τ (brackets denote ensemble averages). The curve fitting for the multi-component model is given by:

$$G(\tau) = 1 + \frac{1}{N}\sum_i y_i \left(1+\frac{\tau}{\tau_i}\right)^{-1}\left(1+\frac{\tau}{s^2\tau_i}\right)^{-\frac{1}{2}}$$

where y_i and τ_i are the fraction and the diffusion time of the component i, respectively; N is the average number of fluorescent molecules in the detection volume defined by the beam waist w_0 and the axial radius z_0; and s is the structure parameter representing the ratio of w_0 and z_0. All $G(\tau)$s in aqueous solutions were measured ten times for 20 s. After pinhole adjustment, diffusion time and structure parameter were determined using a 10^{-7} M rhodamine 6G (Rh6G) solution as a standard before measurements. The values of structural parameters were 6.1–6.6 for GFP and 5.5–6.6 for YFP, respectively. The diffusion constants of fluorescent molecules (D_{sample}) were calculated from the published diffusion constant of Rh6G, D_{Rh6G} (280 μm^2 s^{-1}) and measured diffusion times of Rh6G at the condition (τ_{Rh6G}) and probe proteins (τ_{sample}) as follows:

$$\frac{D_{sample}}{D_{Rh6G}} = \frac{\tau_{Rh6G}}{\tau_{sample}}$$

©2006 Nature Publishing Group

Note: Supplementary Information is available on the Nature Cell Biology website.

ACKNOWLEDGEMENTS

We thank M. Kadota for technical assistance and R. Tsien for providing the mRFP1 plasmid. We are grateful to I. Wada, T. Haraguchi, H. Taguchi, Y. Nagai, T. Shimi, K. Kabayama, K. Saito and H. Fujii for helpful discussion. G.M. was supported by a Human Frontiers Fellowship at Northwestern University and R.I.M. is supported by grants from the National Institutes of Health (National Institute for Medical Science, NIGMS; National Institute for Neurological Diseases and Stroke, NINDS; and National Institute for Aging, NIA), the Huntington Disease Coalition for the Cure, and the Daniel F. and Ada L. Rice Foundation. A.K. and C.P. were supported by fellowships from the Japan Society for Promotion of Science. H.K., M.K. and K.N. were supported by the Grants-in-Aid for Scientific Research programmes in Japan.

COMPETING FINANCIAL INTERESTS

The authors declare that they have no competing financial interests.

Published online at http://www.nature.com/naturecellbiology/
Reprints and permissions information is available online at http://npg.nature.com/reprintsandpermissions/

1. Ross, C. A. Polyglutamine pathogenesis: emergence of unifying mechanisms for Huntington's disease and related disorders. *Neuron* **35**, 819–822 (2002).
2. Gatchel, J. R. & Zoghbi, H. Y. Diseases of unstable repeat expansion: mechanisms and common principles. *Nature Rev. Genet.* **6**, 743–755 (2005).
3. The Huntington's Disease Collaborative Research Group. A novel gene containing a trinucleotide repeat that is expanded and unstable on Huntington's disease chromosomes. *Cell* **72**, 971–983 (1993).
4. DiFiglia, M. *et al.* Huntingtin is a cytoplasmic protein associated with vesicles in human and rat brain neurons. *Neuron* **14**, 1075–1081 (1995).
5. Davies, S. W. *et al.* Formation of neuronal intranuclear inclusions underlies the neurological dysfunction in mice transgenic for the HD mutation. *Cell* **90**, 537–548 (1997).
6. Scherzinger, E. *et al.* Huntingtin-encoded polyglutamine expansions form amyloid-like protein aggregates *in vitro* and *in vivo*. *Cell* **90**, 549–558 (1997).
7. Gidalevitz, T., Ben-Zvi, A., Ho, K. H., Brignull, H. R. & Morimoto, R. I. Progressive disruption of cellular protein folding in models of polyglutamine diseases. *Science* **311**, 1471–1474 (2006).
8. Perutz, M. F., Finch, J. T., Berriman, J. & Lesk, A. Amyloid fibers are water-filled nanotubes. *Proc. Natl Acad. Sci. USA* **99**, 5591–5595 (2002).
9. Young, J. C., Agashe, V. R., Siegers, K. & Hartl, F. U. Pathways of chaperone-mediated protein folding in the cytosol. *Nature Rev. Mol. Cell Biol.* **5**, 781–791 (2004).
10. Muchowski, P. J. & Wacker, J. L. Modulation of neurodegeneration by molecular chaperones. *Nature Rev. Neurosci.* **6**, 11–22 (2005).
11. Fenton, W. A. & Horwich, A. L. Chaperonin-mediated protein folding: fate of substrate polypeptide. *Q. Rev. Biophys.* **36**, 229–256 (2003).
12. Spiess, C., Meyer, A. S., Reissmann, S. & Frydman, J. Mechanism of the eukaryotic chaperonin: protein folding in the chamber of secrets. *Trends Cell Biol.* **14**, 598–604 (2004).
13. Frydman, J. & Hartl, F. U. Principles of chaperone-assisted protein folding: differences between *in vitro* and *in vivo* mechanisms. *Science* **272**, 1497–1502 (1996).
14. Farr, G. W., Scharl, E. C., Schumacher, R. J., Sondek, S. & Horwich, A. L. Chaperonin-mediated folding in the eukaryotic cytosol proceeds through rounds of release of native and nonnative forms. *Cell* **89**, 927–937 (1997).
15. Kubota, H., Hynes, G., Carne, A., Ashworth, A. & Willison, K. Identification of six *Tcp-1*-related genes encoding divergent subunits of the TCP-1-containing chaperonin. *Curr. Biol.* **4**, 89–99 (1994).
16. Llorca, O. *et al.* Eukaryotic chaperonin CCT stabilizes actin and tubulin folding intermediates in open quasi-native conformations. *EMBO J.* **19**, 5971–5979 (2000).
17. Meyer, A. S. *et al.* Closing the folding chamber of the eukaryotic chaperonin requires the transition state of ATP hydrolysis. *Cell* **113**, 369–381 (2003).
18. Nollen, E. A. *et al.* Genome-wide RNA interference screen identifies previously undescribed regulators of polyglutamine aggregation. *Proc. Natl Acad. Sci. USA* **101**, 6403–6408 (2004).
19. Kubota, S., Kubota, H. & Nagata, K. Cytosolic chaperonin protects folding intermediates of Gβ by recognizing hydrophobic β-strands. *Proc. Natl Acad. Sci. USA* **103**, 8360–8365 (2006).
20. Holmberg, C. I., Staniszewski, K. E., Mensah, K. N., Matouschek, A. & Morimoto, R. I. Inefficient degradation of truncated polyglutamine proteins by the proteasome. *EMBO J.* **23**, 4307–4318 (2004).
21. Matsumoto, G., Kim, S. & Morimoto, R. I. Huntingtin and mutant SOD1 form aggregate structures with distinct molecular properties in human cells. *J. Biol. Chem.* **281**, 4477–4485 (2005).
22. Muchowski, P. J. *et al.* Hsp70 and hsp40 chaperones can inhibit self-assembly of polyglutamine proteins into amyloid-like fibrils. *Proc. Natl Acad. Sci. USA* **97**, 7841–7846 (2000).
23. Schaffar, G. *et al.* Cellular toxicity of polyglutamine expansion proteins: mechanism of transcription factor deactivation. *Mol. Cell* **15**, 95–105 (2004).
24. Kim, S., Nollen, E. A., Kitagawa, K., Bindokas, V. P. & Morimoto, R. I. Polyglutamine protein aggregates are dynamic. *Nature Cell. Biol.* **4**, 826–831 (2002).
25. Rigler, R., Mets, U., Widengren, J. & Kask, P. Fluorescence correlation spectroscopy with high count rate and low background: analysis of translational diffusion. *Eur. Biophys. J.* **22**, 169–175 (1993).
26. Terada, S., Kinjo, M. & Hirokawa, N. Oligomeric tubulin in large transporting complex is transported via kinesin in squid giant axons. *Cell* **103**, 141–155 (2000).
27. Feldman, D. E., Spiess, C., Howard, D. E. & Frydman, J. Tumorigenic mutations in VHL disrupt folding *in vivo* by interfering with chaperonin binding. *Mol. Cell* **12**, 1213–1224 (2003).
28. Siegers, K. *et al.* TRiC/CCT cooperates with different upstream chaperones in the folding of distinct protein classes. *EMBO J.* **22**, 5230–5240 (2003).
29. Campbell, R. E. *et al.* A monomeric red fluorescent protein. *Proc. Natl Acad. Sci. USA* **99**, 7877–7882 (2002).
30. Yokota, S., Yanagi, H., Yura, T. & Kubota, H. Cytosolic chaperonin is up-regulated during cell growth. Preferential expression and binding to tubulin at G(1)/S transition through early S phase. *J. Biol. Chem.* **274**, 37070–37078 (1999).

©2006 Nature Publishing Group

nature
cell biology

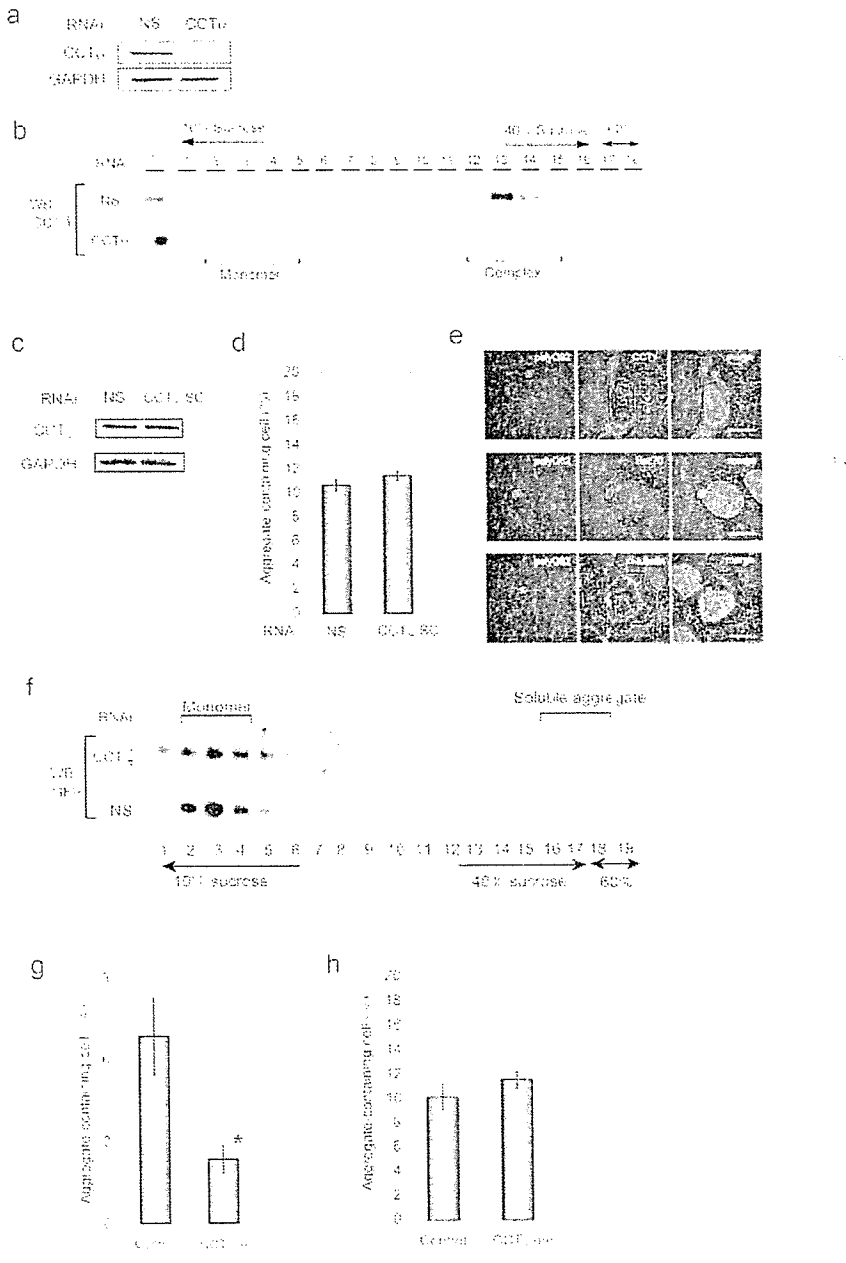

Figure S1 PolyQ aggregation in HEK293 cells under CCT depletion and overexpression conditions. Cells were transfected with CCTα RNAi or nonspecific RNAi vectors and analyzed by western blotting (**a**) or sucrose gradient centrifugation (**b**). Nonspecific RNAi (NS) vector exhibits no difference to CCTζ scrambled RNAi (CCTζ-SC, AAGAGTCGGCTGAGTATCATT) vector for levels of CCTζ protein (**c**) and polyQ aggregation (n=3) (**d**). (**e**) Immunofluorescent staining of CCTγ, HSC70 and α-tubulin in Q82-YFP aggregate containing cells without RNAi treatment. Bar=10 μm. (**f**) Sucrose gradient fractionation of Q82-GFP expressed under CCTζ depleted or normal conditions. Supernatant after centrifugation (600xg, 2 min) was analyzed. Overexpression of all CCT subunits (**g**), but not of CCTζ subunit alone (**h**), inhibits Q82-GFP aggregation (n=3). *, P 0.05.

© 2006 Nature Publishing Group

nature
cell biology

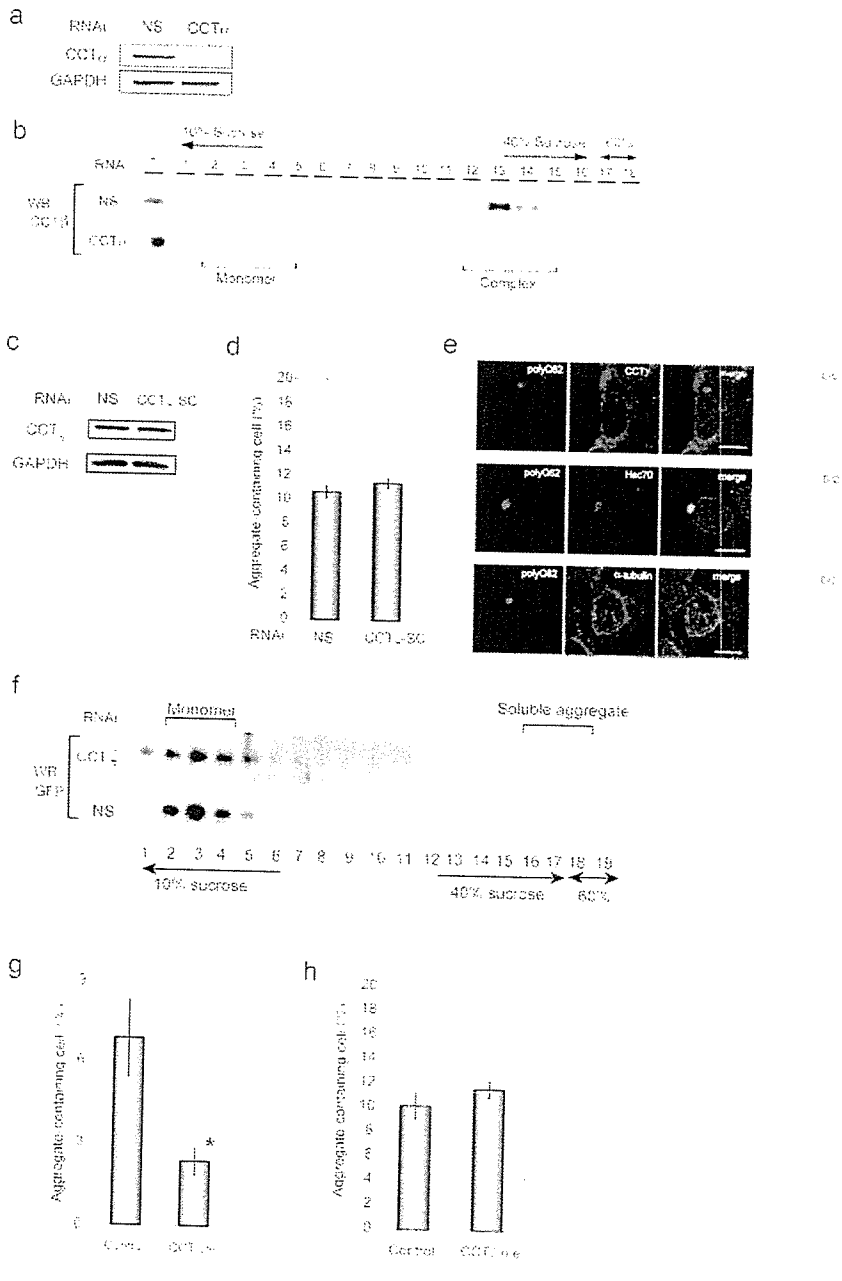

Figure S1 PolyQ aggregation in HEK293 cells under CCT depletion and overexpression conditions. Cells were transfected with CCTα RNAi or nonspecific RNAi vectors and analyzed by western blotting (**a**) or sucrose gradient centrifugation (**b**). Nonspecific RNAi (NS) vector exhibits no difference to CCTζ scrambled RNAi (CCTζ-SC, AAGAGTCGGCTGAGTATCATT) vector for levels of CCTζ protein (**c**) and polyQ aggregation (n=3) (**d**). (**e**) Immunofluorescent staining of CCTγ, HSC70 and α-tubulin in Q82-YFP aggregate containing cells without RNAi treatment. Bar=10 μm. (**f**) Sucrose gradient fractionation of Q82-GFP expressed under CCTζ depleted or normal conditions. Supernatant after centrifugation (600xg, 2 min) was analyzed. Overexpression of all CCT subunits (**g**), but not of CCTζ subunit alone (**h**), inhibits Q82-GFP aggregation (n=3). *, P 0.05.

© 2006 Nature Publishing Group

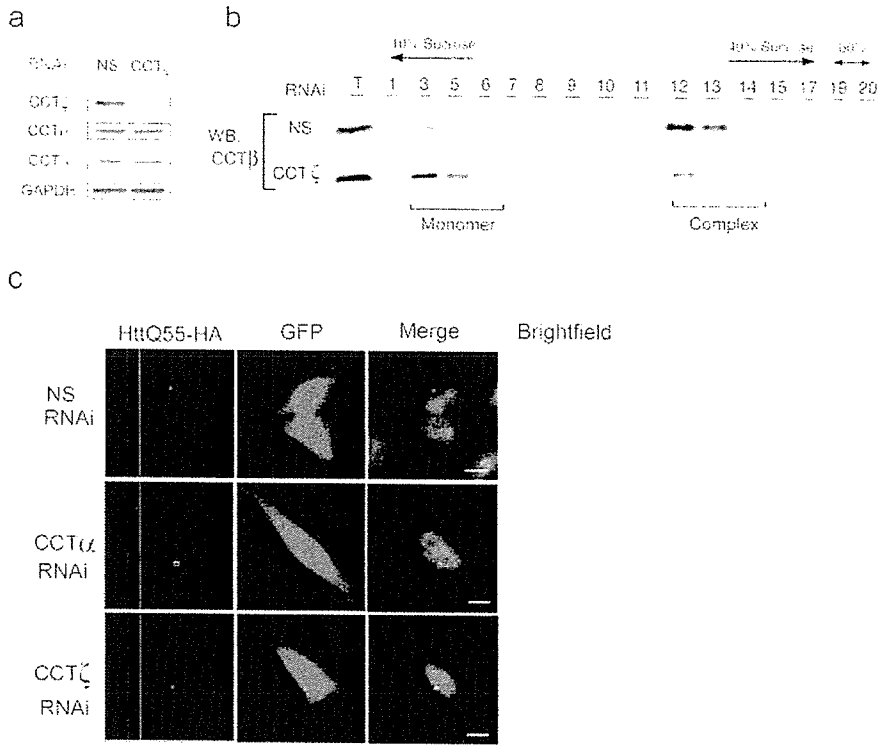

Figure S2 Aggregation of httQ55-HA in HeLa cells under CCT depleted and normal conditions. (**a**) CCTζ-RNAi treatment significantly reduces CCTζ protein. (**b**) Cell extracts were analyzed by sucrose gradient centrifugation. (**c**) Immunofluorescent staining of httQ55-HA aggregates formed under CCT depletion conditions. Bar=10 μm.

© 2006 Nature Publishing Group

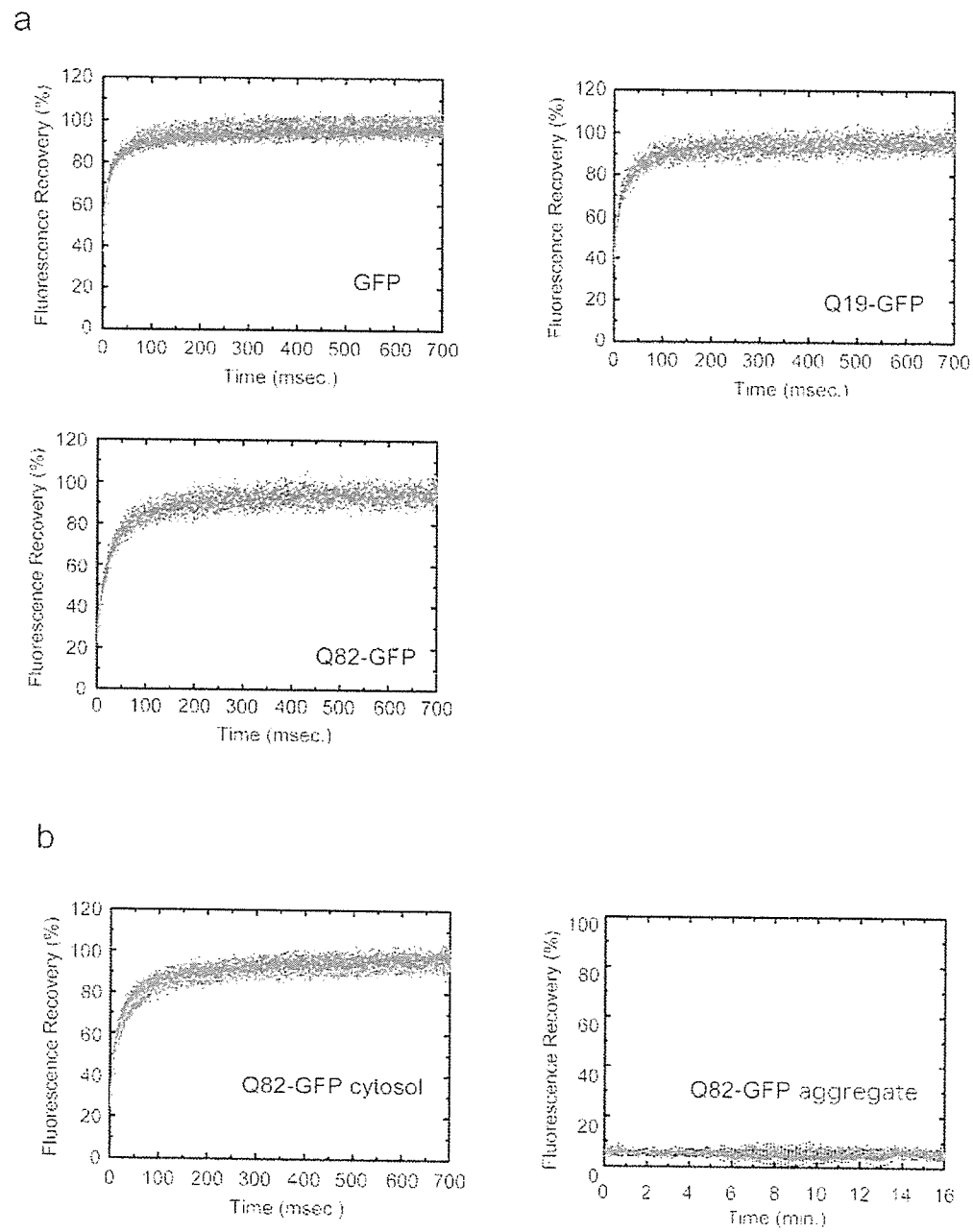

Figure S3 FRAP analysis of polyQ-GFP in HEK293 cells under CCT-depleted conditions at 72 h. Inclusion-free cells (**a**) or inclusion-containing cells (**b**) were analyzed by FRAP[1-3] using Olympus FV1000 (for cytosol) or Carl Zeiss LSM 510 META (for inclusions) confocal microscopes at 37 °C. CCTζ-depleted (green) and control (red) cells were analyzed.

1. Phair, R.D. & Misteli, T. High mobility of proteins in the mammalian cell nucleus. *Nature* **404**, 604-609 (2000).
2. Lippincott-Schwartz, J., Snapp, E. & Kenworthy, A. Studying protein dynamics in living cells. *Nat Rev Mol Cell Biol* **2**, 444-456 (2001).
3. Kimura, H. & Cook, P.R. Kinetics of core histones in living human cells: little exchange of H3 and H4 and some rapid exchange of H2B. *J Cell Biol* **153**, 1341-153 (2001).

© 2006 Nature Publishing Group

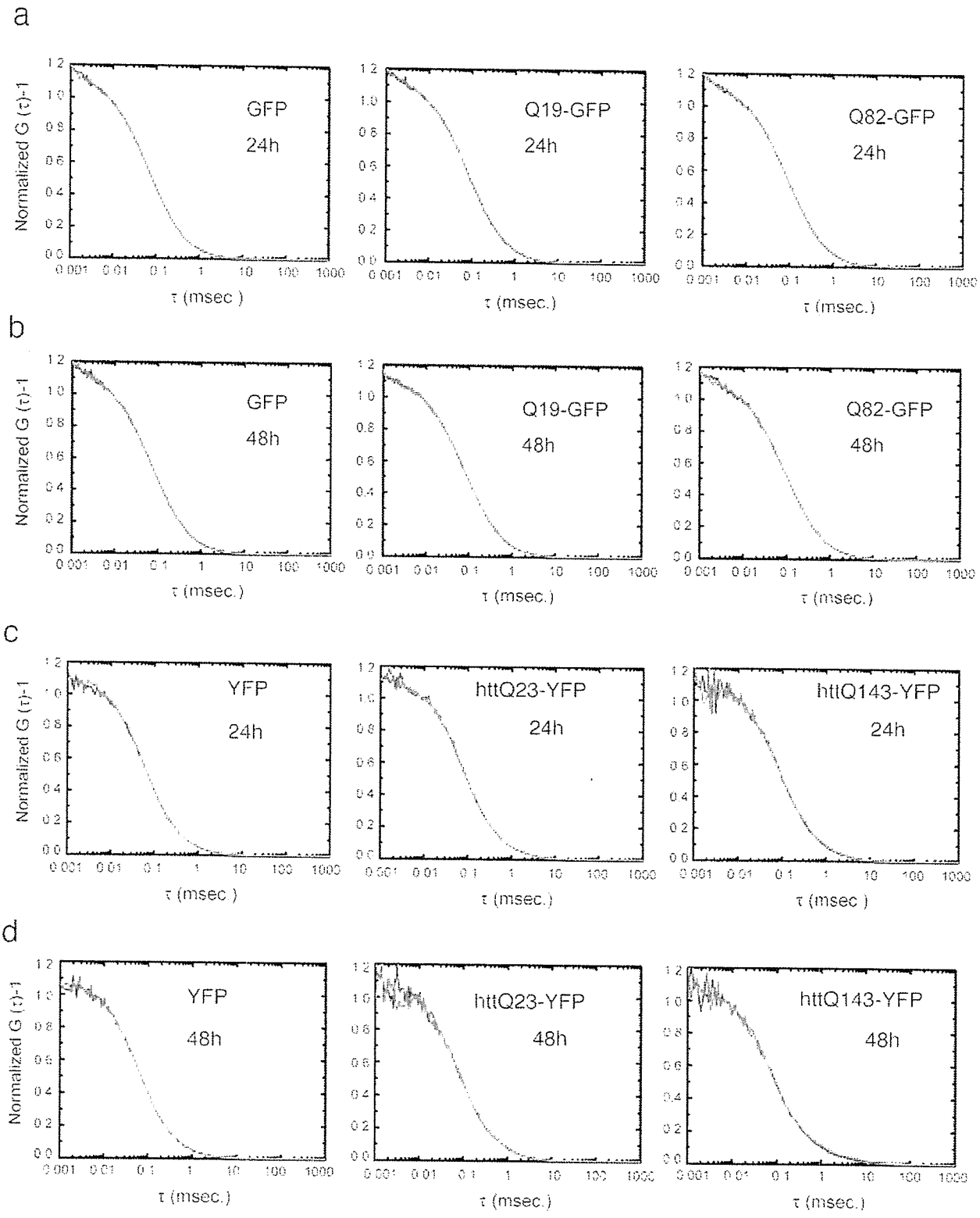

Figure S4 FCS analysis of htt/polyQ proteins under CCT-knockdown conditions at 24 and 48 h. Supernatant after centrifugation (600xg, 2 min) of cell lysate was analyzed. Correlation curves of CCTζ-depleted (red) and control (blue) cells are shown for polyQ-GFP in HEK293 cells after 24 h (**a**) 48 h (**b**) of transfection, or htt-YFP in HeLa cell lines after 24 h (**c**) or 48 h (**d**) of induction.

© 2006 Nature Publishing Group

Full scans of Fig. 1a

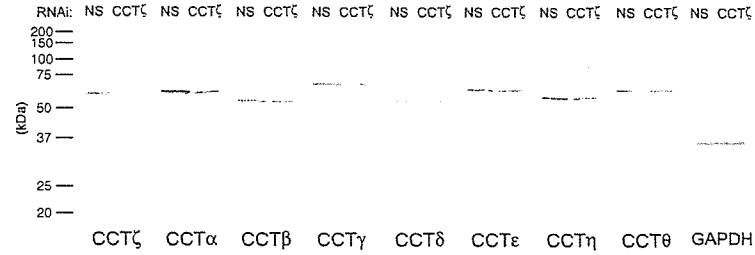

Full scans of Fig. 1b

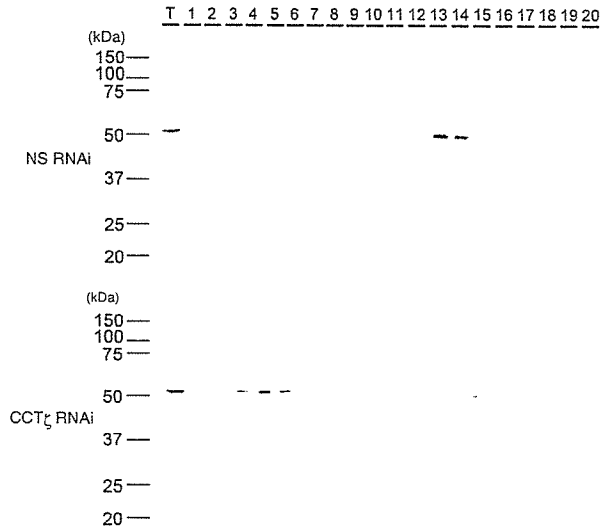

Full scans of Fig. 4e

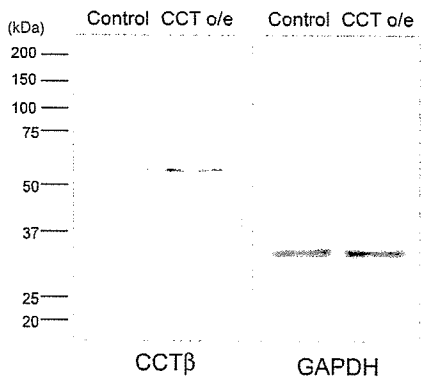

Full scans of Fig. 4f

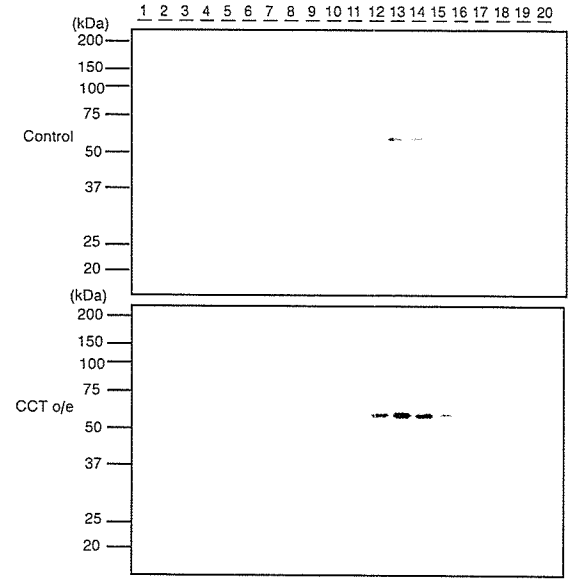

Figure S5 Full scan images of gel/western data.

© 2006 Nature Publishing Group

Dynamics of yeast prion aggregates in single living cells

Shigeko Kawai-Noma[1,a], Satoru Ayano[2,a], Chan-Gi Pack[3], Masataka Kinjo[3], Masasuke Yoshida[4], Kenji Yasuda[2] and Hideki Taguchi[1,*]

[1]*Department of Medical Genome Sciences, Graduate School of Frontier Sciences, University of Tokyo, FSB401, 5-1-5 Kashiwanoha, Kashiwa, Chiba, 277-8562, Japan*

[2]*Department of Life Sciences, Graduate School of Arts and Sciences, University of Tokyo, 3-8-1 Komaba, Meguro-ku, Tokyo, 153-8902 Japan*

[3]*Laboratory of Supramolecular Biophysics, Research Institute of Electronic Sciences, Hokkaido University, N-12 W-6, Kita-ku, Sapporo, 060-0812, Japan*

[4]*Chemical Resources Laboratory, Tokyo Institute of Technology, 4259 Nagatsuta, Yokohama, 226-8503 Japan*

Prions are propagating proteins that are ordered protein aggregates, in which the phenotypic trait is retained in the altered protein conformers. To understand the dynamics of the prion aggregates in living cells, we directly monitored the fate of the aggregates using an on-chip single-cell cultivation system as well as fluorescence correlation spectroscopy (FCS). Single-cell imaging revealed that the visible foci of yeast prion Sup35 fused with GFP are dispersed throughout the cytoplasm during cell growth, but retain the prion phenotype. FCS showed that [PSI$^+$] cells, irrespective of the presence of foci, contain diffuse oligomers, which are transmitted to their daughter cells. Single-cell observations of the oligomer-based transmission provide a link between previous *in vivo* and *in vitro* analyses of the prion and shed light on the relationship between the protein conformation and the phenotype.

Introduction

Prions are infectious proteins (Prusiner 1998; Weissmann 2004). In the prion, the altered conformers of a protein autocatalytically convert the normal structure to the altered form, resulting in deposits of amyloid aggregates. Originally developed from mammalian neurodegenerative diseases, the prion concept has been extended to several non-Mendelian genetic elements in yeast, such as [*PSI*$^+$] and [*URE3*] (Tuite & Cox 2003; Chien *et al.* 2004; Wickner *et al.* 2004; Shorter & Lindquist 2005). Extensive studies over the past decade have revealed that yeast prions are tractable experimental model to investigate prion phenomena.

The budding yeast *Saccharomyces cerevisiae* prion [*PSI*$^+$] (Cox 1965) is a self-propagating altered conformation of the translation termination factor Sup35 (eRF3). The altered polymerized conformation of Sup35 leads to an increased readthrough of stop codons detected as nonsense suppression (Cox 1965). Propagation of [*PSI*$^+$] is dependent on the glutamine/asparagines-rich N-terminal domain of Sup35. *In vivo*, expression of the prion-forming domain of Sup35 fused to GFP (Sup35NM-GFP) in [*PSI*$^+$] cells generates punctate fluorescent aggregates (called foci) (Patino *et al.* 1996), which are often thought to be a hallmark of the prions (Tuite & Cox 2003; Chien *et al.* 2004; Wickner *et al.* 2004; Shorter & Lindquist 2005). *In vitro*, Sup35 fragments containing the N domain form β-sheet rich amyloid aggregates (e.g. Glover *et al.* 1997; King *et al.* 1997; DePace *et al.* 1998; Kishimoto *et al.* 2004; Krzewska & Melki 2006).

Since prions are transmissible, they inherently replicate themselves in order to propagate the transmissible entities. Many attempts have been made to elucidate the transmissible entities in the yeast prion [*PSI*$^+$]. First, several genetic analyses combined with fluorescent microscopic observations have suggested that the fluorescent foci do not directly represent [*PSI*$^+$], since the foci are not always visible in the [*PSI*$^+$] cells (Borchsenius *et al.* 2001; Wegrzyn *et al.* 2001; Zhou *et al.* 2001; Song *et al.* 2005; Wu *et al.* 2005). Second, number of the entities that propagate the [*PSI*$^+$] in yeast (called *propagons*) has been calculated from studies on the kinetics of [*PSI*$^+$] elimination in the presence of guanidine HCl (Eaglestone *et al.* 2000; Cox *et al.* 2003). Finally, recent *in vitro* agarose gel electrophoresis of the [*PSI*$^+$] lysates have shown that

[a]These authors contributed equally.

Communicated by: Yoshikazu Nakamura

Correspondence: E-mail: taguchi@k.u-tokyo.ac.jp

DOI: 10.1111/j.1365-2443.2006.01004.x

© 2006 The Authors
Journal compilation © 2006 by the Molecular Biology Society of Japan/Blackwell Publishing Ltd.

prion aggregates are formed by small Sup35 polymers (8- to 50-mers of Sup35) (Kryndushkin *et al.* 2003).

Although these accumulating studies have illuminated the mechanism by which the prion entities propagate, their conclusions are ambiguous, even confusing, since the conclusions have been based on ensemble experiments. For example, the descriptions of the fluorescent foci have been fluctuating (Wegrzyn *et al.* 2001; Song *et al.* 2005; Wu *et al.* 2005). In addition, there should be a link between the *in vivo* and *in vitro* observations regarding to the molecular entities of the prion. Although recombinant Sup35 amyloid fibrils formed *in vitro* can induce the [*PSI*$^+$] phenotype, the molecular entities critical to the prion propagation as well as relationship between the recombinant Sup35 fibrils and the polymers in the [*PSI*$^+$] lysates revealed by the electrophoresis are unclear.

To overcome the limitation of the ensemble methods, here we monitored the fate of the aggregates using an on-chip single-cell cultivation system together with fluorescence correlation spectroscopy (FCS) (Lippincott-Schwartz *et al.* 2001; Hess *et al.* 2002). Single-cell imaging revealed that the visible foci of yeast prion Sup35 fused with GFP were diffused into the cytoplasm during cell growth, while retaining the prion phenotype. FCS revealed that oligomers of Sup35-GFP were diffused in the cells irrespective of the presence of foci, and then transmitted to their daughter cells as the phenotypic trait. Single-cell observations reveal the dynamical nature of the prion aggregates, which then provides a link between previous *in vivo* and *in vitro* analyses and sheds light on the molecular entities that connect the protein conformation and the phenotype.

Results

On-chip single cultivation system to monitor the fate of the prion aggregates

To monitor the fate of the foci directly we took a single-cell approach using a self-equipped live cell imaging apparatus (Inoue *et al.* 2001a; Umehara *et al.* 2003; Ayano *et al.* 2004), in which individual cells can be continuously observed for long periods of time and the media can be exchanged during cultivation. Micro-chambers for individual yeast cells were fabricated using 30-μm-thick photoresist on 0.2 mm thick glass slides (Supplementary Fig. S1).

We used the 74D-694 [*PSI*$^+$] strain (Tuite & Cox 2003; Wickner *et al.* 2004; Shorter & Lindquist 2005) and transiently induced the expression of Sup35-GFP using the *GAL1* galactose responsive promoter. Single-cell imaging revealed that a typical 4 h induction led to the formation of Sup35-GFP foci in the cytoplasm of [*PSI*$^+$] cells (data not shown). After stopping further induction of Sup35-GFP by exchanging the medium for one lacking galactose, we monitored the fate of the fluorescent foci in real time. Individual live cell imaging showed that the diameter of the foci gradually decreased, and the foci eventually disappeared (Fig. 1A). A statistical analysis revealed that 86% of the foci observed (185 out of 230 cells) were lost, and the half time for disappearance was approximately 2 h (Fig. 1C).

The disappearance of the foci was not due to GFP photobleaching. Even 10 h after we stopped cell growth, by exchanging the synthetic complete (SC) medium with a nutrient-free isotonic buffer, the foci maintained their sizes (Fig. 1B,C). The non-growing cells were not dead, because exchange of the isotonic buffer with SC medium restored growth, and, as in Fig. 1A, the foci disappeared (data not shown). These results, combined with the lack of degradation of the intact Sup35-GFP polypeptides during cell growth (Fig. 1D), indicate that the disappearance of foci is not due to photobleaching or degradation, but due to the dispersal of the foci and Sup35 throughout the cytoplasm of the cell.

The dynamic nature of the foci was not restricted to [*PSI*$^+$] cells. When we conducted similar studies using another yeast prion, [*RNQ1*] (Sondheimer & Lindquist 2000) also known as [*PIN*$^+$] (Derkatch *et al.* 2001; Osherovich & Weissman 2001), cells expressing Rnq1-GFP also lost the Rnq1-GFP foci during cell growth (Supplementary Fig. S2).

Retention of [PSI$^+$] phenotype after the dispersion of the foci

The disappearance of the foci during cell growth raised the question of whether the yeast cells reverted to the non-prion [*psi*$^-$] phenotype during the experimental manipulations, since we cannot distinguish between cells without foci and [*psi*$^-$] cells, because both display diffuse green fluorescence. Thus, we investigated whether the cells maintained the [*PSI*$^+$] phenotype using several approaches. First, a classical genetic test using a [*PSI*$^+$]-mediated nonsense suppression was conducted (Cox 1965). Typically, [*PSI*$^+$] cells grow in medium lacking adenine (SC-Ade) and the colonies appear white on SC medium, whereas [*psi*$^-$] cells cannot grow in SC-Ade and the colonies appear red on SC. Under conditions in which the foci disappeared, the colony color was white, and the cells were viable on SC-Ade (Fig. 2A), indicating that the [*PSI*$^+$] phenotype was maintained after the foci disappeared. Secondly, we developed a nonsense suppression assay to distinguish the prion phenotype in

© 2006 The Authors
Journal compilation © 2006 by the Molecular Biology Society of Japan/Blackwell Publishing Ltd.

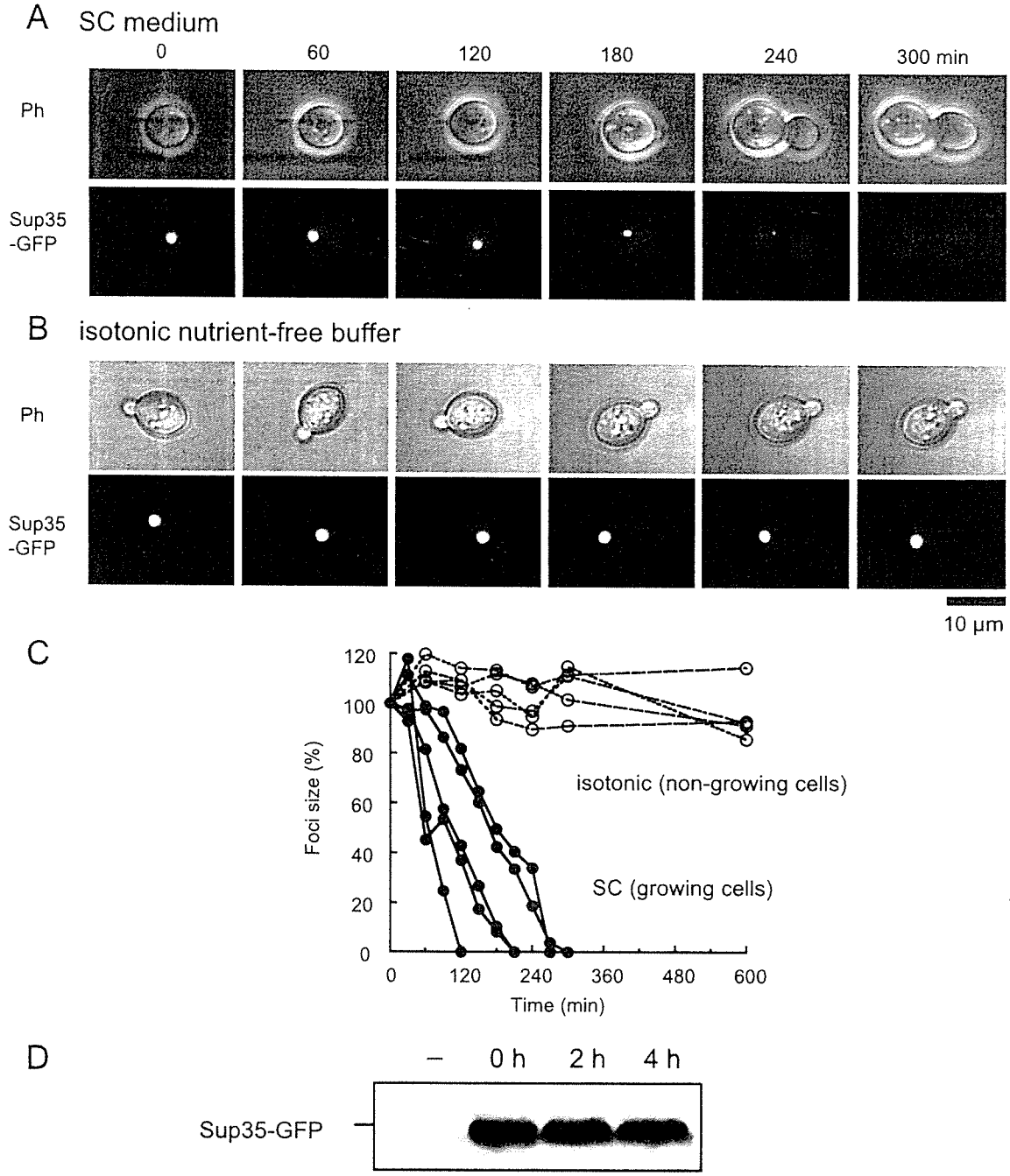

Figure 1 Dynamics of the Sup35NM-GFP foci in individual living cells detected using the on-chip cultivation system. (A, B) Time-lapse imaging of living [*PSI*$^+$] cells cultured in (A) SC medium and (B) an isotonic nutrient-free buffer. Phase contrast (Ph) and fluorescent images are shown. After the formation of Sup35NM-GFP foci induced by SC containing galactose, the medium was exchanged to SC or the isotonic buffer. Images show single z-sections, but we confirmed the absence of the foci in all z-sections when the foci disappeared in the section being observed. (C) Foci size measurements in individual [*PSI*$^+$] cells cultured in SC (closed symbols) or isotonic buffer (open symbols). Cross-sectional areas of the fluorescent foci were digitally determined. Sizes of the foci at 0 min from the medium exchange were set to 100%. (D) The Sup35NM-GFP fusion protein was not degraded during the observation time. The cultured [*PSI*$^+$] cells in rich medium were collected before (–) and after (0, 2, 4 h) the induction of Sup35NM-GFP. After cell lysis, the lysates were separated by 10% SDS-PAGE. Sup35NM-GFP and a loading control, enolase were detected with anti-Sup35NM serum and anti-yeast enolase serum, respectively. Only the bands of Sup35NM-GFP are shown.

© 2006 The Authors
Journal compilation © 2006 by the Molecular Biology Society of Japan/Blackwell Publishing Ltd.

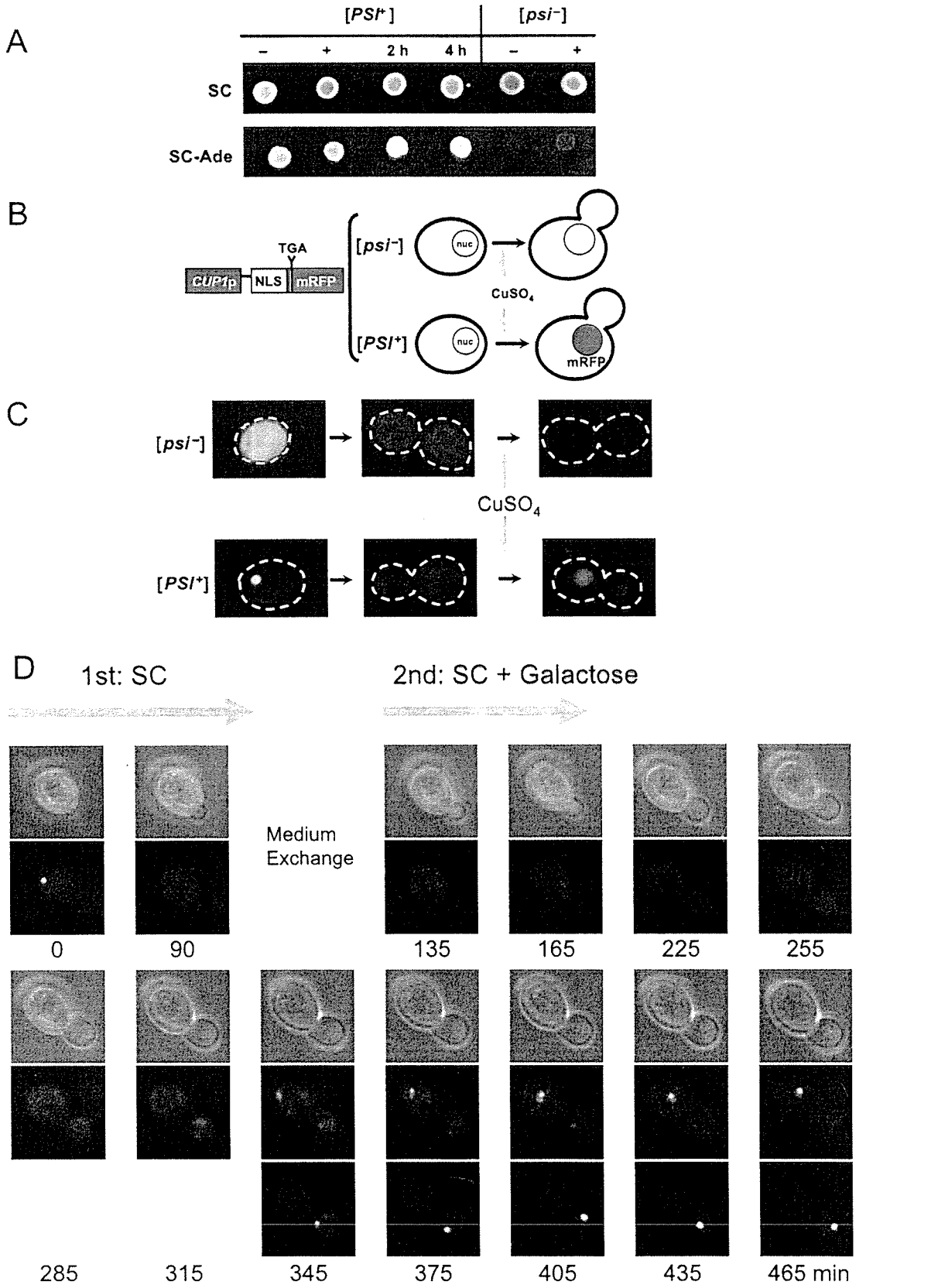

© 2006 The Authors
Journal compilation © 2006 by the Molecular Biology Society of Japan/Blackwell Publishing Ltd.

individual living cells, as shown schematically in Fig. 2B. [*PSI*$^+$] cells were transformed with a plasmid encoding a Cu^{2+}-inducible monomeric red fluorescent protein (mRFP) (Campbell *et al.* 2002), with an N-terminal nuclear localization signal (NLS-mRFP) and a stop codon in the coding region, to monitor nonsense suppression. Although this fluorescent reporter assay is similar to that developed by Satpute-Krishnan & Serio (2005) using GST-DsRed fusion protein, our assay system results in an accumulation of red fluorescence in the nucleus in [*PSI*$^+$] cells. After the foci disappeared in [*PSI*$^+$] cells (as shown in Fig. 1A), the addition of Cu^{2+} resulted in red fluorescence in more than 10% of the nuclei, whereas no red fluorescence was observed in [*psi*$^-$] cells (Fig. 2C). Finally, the punctate foci reappeared when Sup35-GFP was re-induced (Fig. 2D), indicating that the nucleating sites of the foci were not lost in cells after the foci disappeared. Moreover, Fig. 2D also shows the appearance of the foci in the daughter cell at almost same time as when the foci re-appeared in the mother cell, indicating that the nucleating sites are transmitted from the mother to daughter cell. We conclude that the [*PSI*$^+$] prion phenotype was maintained in cells even in the absence of foci, and therefore we refer to the [*PSI*$^+$] cells without foci as [*PSI*$^+$(−foci)] cells.

Fluorescence correlation spectroscopy (FCS) to analyze the size of prion aggregates in living cells

Next, we measured the size of the diffused Sup35-GFP aggregates in the [*PSI*$^+$(−foci)] cells by exploiting fluorescence correlation spectroscopy (FCS). FCS is a technique to determine the diffusion times of fluorescence molecules by calculating the autocorrelation function in a microscopic detection volume under 10^{-15} L (1 femtoliter) defined by a tightly focused laser beam and pinhole (Lippincott-Schwartz *et al.* 2001; Hess *et al.* 2002), providing us an estimation of the size of aggregates. Since FCS is usually combined with confocal laser scanning microscopy (LSM), we can define the detection volume at any position of interest inside a living cell in a non-invasive manner (Lippincott-Schwartz *et al.* 2001; Hess *et al.* 2002).

Prior to the application of FCS to the yeast prion, we tested whether FCS is applicable to living yeast cells since published FCS data are not available for the budding yeast system. Typical fluorescence autocorrelation functions (FAFs) of monomeric GFP (not fused to Sup35) in yeast lysates (solutions) and living cells of [*PSI*$^+$] and [*psi*$^-$] are shown in Fig. 3A. FAFs of monomeric GFP in the lysates of [*PSI*$^+$] and [*psi*$^-$] were well fitted by an one-component model. Estimated diffusion times of monomeric GFP in the lysates (~80 μs) were consistent with those described in a previous FCS result (Saito *et al.* 2003). Compared with the FAFs of GFP in lysates, FAFs of GFP in living cells were shifted to the right, indicating slower diffusional mobility within the cell, which was mainly due to the high viscosity of the yeast cytoplasm. Diffusion profiles of GFP molecules in [*PSI*$^+$] and [*psi*$^-$] cells were almost the same, reflecting indistinguishable viscosities in the cytoplasm of [*PSI*$^+$] and [*psi*$^-$]. FAFs of GFP in the cell were fitted by a two-component model. More than 90% of the species were fast-moving, corresponding to the monomeric form of GFP with diffusion times of 300–400 μs.

After confirming that FCS was applicable to living yeast cells, we measured the fluorescence fluctuations of Sup35-GFP in the cytoplasm of individual cells (Fig. 3B). The autocorrelation decays of Sup35-GFP in [*psi*$^-$] cells (Fig. 3B) were almost the same as those in cells expressing the GFP monomer alone (Fig. 3A), indicating that the [*psi*$^-$] cells contain mostly monomers of Sup35-GFP. In [*PSI*$^+$(+foci)] cells, we focused the laser on a cytoplasmic region lacking foci. We could not determine the diffusion profiles of the foci themselves. The principle of FCS, in which only freely diffusing molecules are subjects for the measurements, does not allow the measurement of virtually immobilized molecules, such as the foci. The autocorrelation decays of the [*PSI*$^+$(+foci)] cells exhibited slower profiles than those of the [*psi*$^-$] cells, indicating that the Sup35-GFP species in [*PSI*$^+$(+foci)] cells were much larger than those in [*psi*$^-$] cells. We then measured the autocorrelation functions of [*PSI*$^+$(−foci)] cells and found that the autocorrelation

Figure 2 Maintenance of the [*PSI*$^+$] phenotype after disappearance of the foci. (A) Conventional assay for nonsense suppressor phenotype. Yeast cells were plated on either SC or SC without adenine (SC-Ade) plates. Photographs were taken after cultivation for 3 days at 30 °C. The [*psi*$^-$] cells were also plated as a control. (B,C) Single-cell read-through assay. (B) Schematic representation of the assay. A stop codon was introduced in a Cu^{2+}-inducible monomeric RFP fused to an N-terminal nuclear localization signal (NLS-mRFP). After induction of the NLS-mRFP, the [*PSI*$^+$]-dependent read-through leads to the accumulation of red fluorescence in the nucleus. (C) Typical results of the read-through assay. In the [*PSI*$^+$] cells, Cu^{2+} was added after the Sup35-GFP foci disappeared. (D) Re-appearance of the Sup35-GFP foci. First, [*PSI*$^+$] cells bearing fluorescent foci were cultured in SC medium to allow the foci to disappear, as shown in Fig. 1A. After confirmation of the disappearance, the medium was exchanged to SC containing galactose to induce Sup35-GFP. To show the re-appearance of foci, which appeared at almost the same time in both daughter and mother cells, two fluorescent images at different focal planes are shown from 345 min.

© 2006 The Authors
Journal compilation © 2006 by the Molecular Biology Society of Japan/Blackwell Publishing Ltd.

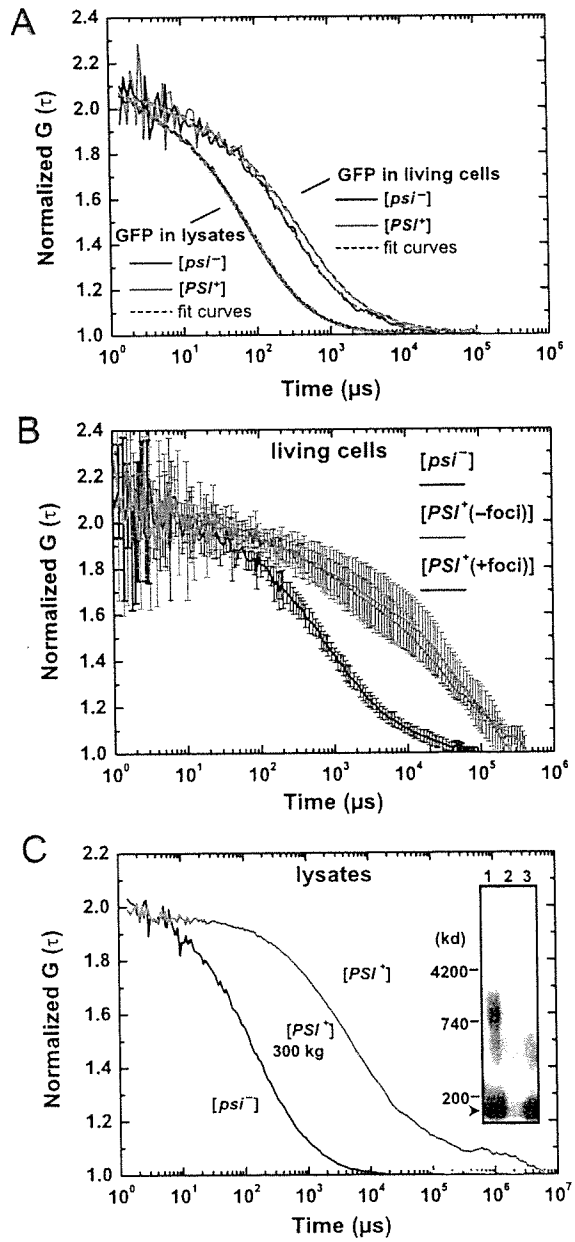

Figure 3 Fluorescence correlation spectroscopy (FCS) measurement of yeast prion aggregates. (A) Normalized autocorrelation curves of monomeric GFP (not fused with Sup35NM) in lysates and living yeast cells. Diffusion profiles of GFP in the lysates and cytoplasm of [*psi*$^-$] and [*PSI*$^+$] cells were measured. The autocorrelation curves in the lysates and cells are fitted by one-component model and two-component model, respectively (*dotted lines*). The ratios of diffusion times in the cells (major component) to those in the lysates (solutions) (τ_{cell}/τ_{sol}), which allows calculation of the apparent viscosity ratio, η_{cell}/η_{sol} (Equation 4 in Experimental procedures), were approximately 4.3 for [*psi*$^-$] cell and 5.5 for [*PSI*$^+$] cell, respectively. (B) Normalized autocorrelation curves of Sup35-GFP in living yeast cells. Diffusion profiles of Sup35-GFP in the cytoplasm of [*psi*$^-$], [*PSI*$^+$(+foci)], and [*PSI*$^+$(–foci)] cells were measured. The mean ± standard deviations of six independent measurements are shown. (C) Comparison of FCS data with aggregate size measured by semidenaturing agarose gel electrophoresis (inset) of yeast lysates. Yeast lysates obtained from [*PSI*$^+$] (*lane 1*) and [*psi*$^-$] (lane 3) cells, and the supernatant from [*PSI*$^+$] lysate centrifuged at 300 kg (lane *2*) were analyzed either by FCS or by electrophoresis. Anti-Sup35NM was used for Western blotting detection. The arrowhead shows the position of the Sup35-GFP monomer. In each panel, the amplitudes of autocorrelation functions were normalized to 2 in order to easily compare the diffusion profiles.

profiles of [*PSI*$^+$(–foci)] cells were indistinguishable from those of [*PSI*$^+$(+foci)] cells (Fig. 3B). Moreover, we also examined other [*PSI*$^+$] cells, [*GPSI*$^+$], in which GFP is inserted between the N and M domains of the endogenous Sup35 (Sup35-NGMC) (Song *et al.* 2005; Wu *et al.* 2005), with FCS. Again, the Sup35-NGMC in [*GPSI*$^+$] cells was larger than that in [*Gpsi*$^-$] cells, confirming that endogenous Sup35 also exists in an oligomeric state (Supplementary Fig. S3). These results indicate that the larger species, referred to here as diffuse oligomers, are dispersed in the cytoplasm of [*PSI*$^+$] cells, regardless of the presence of foci.

In addition to the live cell FCS analyses, *in vitro* FCS measurements using the cell lysates also gave different diffusion profiles between [*PSI*$^+$] and [*psi*$^-$] (Fig. 3C). We found that the Sup35-GFP molecules in the [*PSI*$^+$] lysate moved much more slowly than those in the [*psi*$^-$] lysate (Fig. 3C), indicating that larger aggregates of Sup35-GFP exist in the [*PSI*$^+$] lysate. Since a recent biochemical analysis using agarose gel electrophoresis suggested that relatively small Sup35 oligomers are responsible for prion propagation (Kryndushkin *et al.* 2003), we analyzed the lysates by electrophoresis. As described by Kryndushkin *et al.* (2003), we also observed 740–4200 kDa Sup35-GFP oligomers in the [*PSI*$^+$] lysate (Fig. 3C inset, lane 1), which were almost entirely removed by centrifugation at 300 kg for 25 min (Fig. 3C inset, lane 2). In the FCS analysis, the supernatant of the centrifuged sample shifted the diffusion profile of the [*PSI*$^+$] lysate to the left, and it almost overlapped with the [*psi*$^-$] lysate (Fig. 3C). Therefore, we concluded that the slower diffusion of Sup35-GFP in the [*PSI*$^+$] lysate was due to the 740–4200 kDa oligomers identified by the electrophoresis.

Direct observation of the oligomer-based transmission to the daughter cells revealed by time-lapse FCS

The non-invasive character of FCS allowed us to focus the laser in daughter cells. We developed a time-lapse FCS system, using the on-chip cultivation system to

© 2006 The Authors
Journal compilation © 2006 by the Molecular Biology Society of Japan/Blackwell Publishing Ltd.

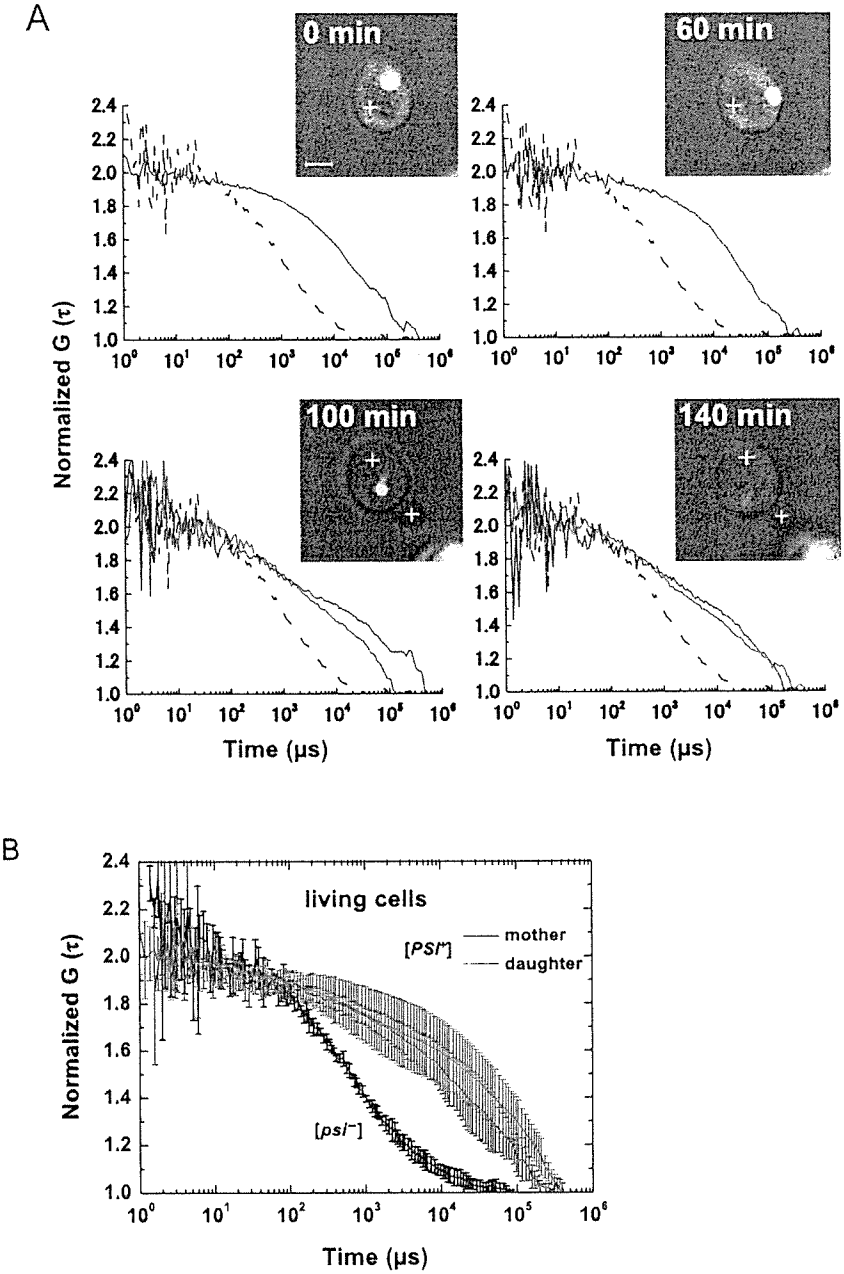

Figure 4 Transmission of the diffuse oligomers from mother to daughter cell. (A) Autocorrelation functions of mother (blue) and daughter (red) cells obtained by time-lapse FCS measurements. An FCS apparatus equipped with the on-chip microculture system was used to cultivate yeast cells. FCS data of a single [*PSI*$^+$ (+foci)] cell were repeatedly measured during the cell growth. The formation of the [*PSI*$^+$(+foci)] cell was as in Fig. 1A. Images in insets show the confocal and light microscopic images (merged) of the growing yeast cell used for the time-lapse FCS analysis. The cross hairs (+) show the positions of the FCS measurements. The averaged autocorrelation function of Sup35-GFP in [*psi*$^-$] cells is shown as a reference (dotted line). (B) Averaged autocorrelation functions of Sup35-GFP in the mother (blue) and daughter (red) [*PSI*$^+$] cells. FCS data were measured after the appearance of the foci.

measure the size of the Sup35-GFP in the daughter cells immediately after transmission from the mother [*PSI*$^+$] cells. Autocorrelation functions of both the mother and daughter cells were measured as the [*PSI*$^+$(+foci)] cell was budding (Fig. 4A), under the conditions shown in Fig. 1A). Strikingly, the autocorrelation function of Sup35-GFP in the daughter cell in an early budding step (Fig 4A, 100 min) was almost the same as that in the mother cell, indicating that the diffuse oligomers are transmissible to daughter cells. On average, the diffusion profiles of Sup35-GFP in the daughter cells were almost identical to those of the mother [*PSI*$^+$] cells (Fig. 4B). These time-lapse FCS results, combined with the retention of the nucleating sites in the daughter cells (Fig. 2D), demonstrate that the oligomeric species dispersed in the mother cells are directly transmitted to their daughter cells.

Discussion

Since prions are propagating proteins, how the prion entity is transmitted from cell to cell is central to prion

© 2006 The Authors
Journal compilation © 2006 by the Molecular Biology Society of Japan/Blackwell Publishing Ltd.

biology. To address the central question, we took two powerful approaches, an on-chip microcultivation system and FCS. The introduction of the two single-cell approaches enabled us to visualize the dynamic nature of prion entities, which cannot be extracted from the experiments based on ensembles of cells in a population. Furthermore, using the time-lapse FCS technique, we directly observed the oligomer-based transmission of yeast prion from the mother to the daughter cell. Although some earlier studies have described the related issue we focused in this study, we consider that our study has decisive advances over the earlier studies as discussed below.

Previous ensemble experiments have suggested that the fluorescent foci are not responsible for [*PSI*$^+$] (Borchsenius *et al.* 2001; Wegrzyn *et al.* 2001; Zhou *et al.* 2001; Song *et al.* 2005; Wu *et al.* 2005). Using the single-cell approaches we directly demonstrated that this is the case. In addition, we clearly observed that the dynamics of the foci, in which the foci were dispersed into the cytoplasm during the cell growth. Relating to this issue, Wu *et al.* (2005) have recently reported the dynamics of the Sup35-GFP foci after the addition of guanidine HCl, which is known to cure [*PSI*$^+$]. Our single-cell analysis of Sup35 aggregates clearly revealed that, even in the absence of guanidine HCl, the foci dynamically dispersed into the oligomers, which are large enough to maintain their phenotypical characteristics.

The general understanding on the foci based on the ensemble experiments is one of logical consequences, and thus there is some confusion in the earlier papers. For example, one of the papers has suggested that the foci are dead-end products (Wegrzyn *et al.* 2001) which is obviously contrary to our conclusion. Another is that the descriptions of the fluorescent foci in two recent publications by the same authors have been different (Song *et al.* 2005; Wu *et al.* 2005). The confusion was settled by our clear-cut observations, providing further progress in the prion field.

The findings that the "visible" aggregates (the foci) are not necessary for the prion propagation, suggested by the previous papers, would imply the potential importance of the "invisible" species. We successfully extracted information from the "invisible" entities by using state-of-the-art FCS technique. Dynamical character of the "invisible" fluorescent molecules in cells can be also measured by other technique, fluorescent recovery after photobleaching (FRAP), which has been already applied to Sup35-GFP analysis (Song *et al.* 2005; Wu *et al.* 2005). FCS has several advantages such as high sensitivity, broad dynamic range and potential quantitative analysis, compared to FRAP. In particular, FCS has a potential to measure a total number of fluorescent molecules contained in the defined volume, although we did not analyze it because of several technical difficulties at present status. In the near future, FCS is promising to quantitate the number of the prion entities, leading to a direct demonstration of previously estimated number of propagating entities called *propagons* (Eaglestone *et al.* 2000; Cox *et al.* 2003).

Since FCS enables us to extract the information on the prion entities even in living cells, we can investigate the propagating prions at the molecular level. A growing number of studies have analyzed the prion aggregates in the lysates using the semidenaturing agarose gel electrophoresis (Kryndushkin *et al.* 2003; Bagriantsev & Liebman 2004; Salnikova *et al.* 2005; Borchsenius *et al.* 2006; Shkundina *et al.* 2006). As shown in Fig. 3, FCS analyses shown here provided a link between the *in vivo* and *in vitro* observations, and shed new light on the relationship between the altered conformations and the phenotype in living cells. One of the most intriguing questions is that the size of the diffused oligomers *in vivo*. Although FCS can approach this important question by fitting the autocorrelation curves, we have failed to obtain reliable values on the sizes of the oligomers, due to possible heterogeneous populations with unknown shape of the oligomers. Relating to this question, purified Sup35 easily forms long fibrils that can reach a length longer than the diameter of a yeast cell (e.g. Glover *et al.* 1997; Inoue *et al.* 2001b), but so far, such filaments have not been observed *in vivo*. Future quantitative FCS analysis, such as a distribution analysis of diffusion constants, might provide answers for several basic questions about the sizes and shapes of Sup35 aggregates inside the living cells.

The conclusions presented here are not restricted to yeast prions, but are also related to recent studies on other protein aggregates. The dynamic nature of polyglutamine aggregates has been reported (Kim *et al.* 2002), and there is a growing body of evidence that the inherent toxicity of protein aggregates is caused by the oligomeric forms, not large aggregates (Bucciantini *et al.* 2002; Kayed *et al.* 2003; Cleary *et al.* 2005; Silveira *et al.* 2005). The single-cell approach described here is a useful tool for further characterization of the oligomeric forms of proteins inside living cells, which is essential to understand the cellular function of the protein aggregates.

Experimental procedures

Yeast strains and media

The strains used in this study were 74-D694 (*MAT***a** *ade1-14 leu2-3112 his3-Δ200 trp1-289 ura3-52* [*PSI*$^+$] or [*psi*$^-$]). Standard rich

© 2006 The Authors
Journal compilation © 2006 by the Molecular Biology Society of Japan/Blackwell Publishing Ltd.